

# Development of a scattering model for diatomic gas-solid surface interactions by an unsupervised machine learning approach

**Citation for published version (APA):**

Mohammad Nejad, S., Gaastra-Nedea, S. V., Frijns, A. J. H., & Smeulders, D. M. J. (2022). Development of a scattering model for diatomic gas-solid surface interactions by an unsupervised machine learning approach. *Physics of Fluids*, 34(11), Article 117122. <https://doi.org/10.1063/5.0110117>

**DOI:**

[10.1063/5.0110117](https://doi.org/10.1063/5.0110117)

**Document status and date:**

Published: 17/11/2022

**Document Version:**

Publisher's PDF, also known as Version of Record (includes final page, issue and volume numbers)

**Please check the document version of this publication:**

- A submitted manuscript is the version of the article upon submission and before peer-review. There can be important differences between the submitted version and the official published version of record. People interested in the research are advised to contact the author for the final version of the publication, or visit the DOI to the publisher's website.
- The final author version and the galley proof are versions of the publication after peer review.
- The final published version features the final layout of the paper including the volume, issue and page numbers.

[Link to publication](#)

**General rights**

Copyright and moral rights for the publications made accessible in the public portal are retained by the authors and/or other copyright owners and it is a condition of accessing publications that users recognise and abide by the legal requirements associated with these rights.

- Users may download and print one copy of any publication from the public portal for the purpose of private study or research.
- You may not further distribute the material or use it for any profit-making activity or commercial gain
- You may freely distribute the URL identifying the publication in the public portal.

If the publication is distributed under the terms of Article 25fa of the Dutch Copyright Act, indicated by the "Taverne" license above, please follow below link for the End User Agreement:

[www.tue.nl/taverne](http://www.tue.nl/taverne)

**Take down policy**

If you believe that this document breaches copyright please contact us at:

[openaccess@tue.nl](mailto:openaccess@tue.nl)

providing details and we will investigate your claim.


# Development of a scattering model for diatomic gas–solid surface interactions by an unsupervised machine learning approach

Cite as: Phys. Fluids **34**, 117122 (2022); <https://doi.org/10.1063/5.0110117>

Submitted: 15 July 2022 • Accepted: 27 September 2022 • Accepted Manuscript Online: 29 September 2022 • Published Online: 17 November 2022

 Shahin Mohammad Nejad,  Silvia Nedeia,  Arjan Frijns, et al.

## COLLECTIONS

 This paper was selected as Featured



View Online



Export Citation



CrossMark

## ARTICLES YOU MAY BE INTERESTED IN

[A review on deep reinforcement learning for fluid mechanics: An update](#)

Physics of Fluids **34**, 111301 (2022); <https://doi.org/10.1063/5.0128446>

[Effects of spanwise length and side-wall boundary condition on plunging breaking waves](#)

Physics of Fluids **34**, 112125 (2022); <https://doi.org/10.1063/5.0124895>

[Pore-scale study of mineral dissolution in heterogeneous structures and deep learning prediction of permeability](#)

Physics of Fluids **34**, 116609 (2022); <https://doi.org/10.1063/5.0123966>



## Physics of Fluids

### Special Topic: Food Physics

**Submit Today!**

# Development of a scattering model for diatomic gas–solid surface interactions by an unsupervised machine learning approach

Cite as: Phys. Fluids **34**, 117122 (2022); doi: [10.1063/5.0110117](https://doi.org/10.1063/5.0110117)

Submitted: 15 July 2022 · Accepted: 27 September 2022 ·

Published Online: 17 November 2022



View Online



Export Citation



CrossMark

Shahin Mohammad Nejad,  Silvia Nedeia,  Arjan Frijns, <sup>a)</sup>  and David Smeulders 

## AFFILIATIONS

Department of Mechanical Engineering, Eindhoven University of Technology, P.O. Box 513, 5600 MB Eindhoven, The Netherlands

<sup>a)</sup> Author to whom correspondence should be addressed: [a.j.h.frijns@tue.nl](mailto:a.j.h.frijns@tue.nl)

## ABSTRACT

This work proposes a new stochastic gas–solid scattering model for diatomic gas molecules constructed based on the collisional data obtained from molecular dynamics (MD) simulations. The Gaussian mixture (GM) approach, which is an unsupervised machine learning approach, is applied to H<sub>2</sub> and N<sub>2</sub> gases interacting with Ni surfaces in a two-parallel wall system under rarefied conditions. The main advantage of this approach is that the entire translational and rotational velocity components of the gas molecules before and after colliding with the surface can be utilized for training the GM model. This creates the possibility to study also highly nonequilibrium systems and accurately capture the energy exchange between the different molecular modes that cannot be captured by the classical scattering kernels. Considering the MD results as the reference solutions, the performance of the GM-driven scattering model is assessed in comparison with the Cercignani–Lampis–Lord (CLL) scattering model in different benchmarking systems: the Fourier thermal problem, the Couette flow problem, and a combined Fourier–Couette flow problem. This assessment is performed in terms of the distribution of the velocity components and energy modes, as well as accommodation coefficients. It is shown that the predicted results by the GM model are in better agreement with the original MD data. Especially, for H<sub>2</sub> gas the GM model outperforms the CLL model. The results for N<sub>2</sub> molecules are relatively less affected by changing the thermal and flow properties of the system, which is caused by the presence of a stronger adsorption layer.

© 2022 Author(s). All article content, except where otherwise noted, is licensed under a Creative Commons Attribution (CC BY) license (<http://creativecommons.org/licenses/by/4.0/>). <https://doi.org/10.1063/5.0110117>

## I. INTRODUCTION

Rarefied gas dynamics or the methods of discrete molecular gas dynamics are applied in various cutting-edge technologies, such as aerodynamics of the hypersonic vehicles, semiconductor industry, micro-electro-mechanical systems, and micro/nanoporous media.<sup>1</sup> In the aforementioned applications, usually the mean free path ( $\lambda$ ) of the gas molecules and the characteristic dimension ( $d$ ) of the system are in the same order of magnitude. This implies that knowing the details of discrete molecular behavior becomes of crucial importance in understanding flow physics. By increasing the degree of rarefaction, quantified by means of the Knudsen number ( $Kn = \frac{\lambda}{d}$ ), interactions between gas molecules and the adjacent solid surfaces become more dominant than intermolecular gas–gas collisions in determining the macroscopic gas flow characteristics.<sup>2,3</sup> Accordingly, it is well established that for  $Kn > 0.1$  gas experiences significant nonequilibrium phenomena, such as velocity slip and temperature jump at the vicinity of the surface in the region known as the Knudsen layer. As a result, the continuum

Navier–Stokes equations are not applicable anymore to describe flow properties.<sup>3,4</sup> Particle-based numerical techniques, such as direct simulation Monte Carlo (DSMC) method<sup>5</sup> and lattice Boltzmann method (LBM),<sup>6</sup> are being extensively employed for simulating rarefied gas flows. In addition to gas–gas molecular collision models, the successful application of these numerical techniques depends upon the development of accurate gas–surface interaction (GSI) models. However, despite devoting considerable efforts over the last century toward developing realistic GSI models,<sup>7–16</sup> the physics of GSI phenomena are still not well understood, and reliable and generalized GSI models to describe complex surface interactions and highly nonequilibrium flow in modern engineering applications are still lacking.

In accordance with the probabilistic essence of the particle-based numerical approaches, all commonly used GSI models have also been presented in probabilistic forms describing the relationship between the state of gas molecules before and after colliding with the surface.<sup>2</sup> Generally, according to these models, it can be assumed that the state

of scattered molecules falls between two extreme situations: purely specular and purely diffuse reflections. The proportion of diffuse scattering is determined by the so-called accommodation coefficient (AC), which is a parameter to quantify the amount of momentum or thermal energy exchange between gas and solid. The Maxwell model<sup>7</sup> is the simplest empirical GSI model, in which only the tangential momentum AC is used in the model. It assumes that a fixed amount of gas molecules undergoes a fully diffuse reflection, while the remaining part reflects specularly. However, Cercignani and Lampis<sup>9</sup> observed that the Maxwell model was not able to capture the lobular patterns seen in the molecular beam experiment. To tackle this deficiency, they used the normal energy AC alongside the tangential momentum AC and established a more realistic and mathematically more robust GSI model that better matched with experimental data. The so-called Cercignani-Lampis (CL) model was extended by Lord,<sup>10</sup> who proposed the well-known Cercignani-Lampis-Lord (CLL) model and applied it into the DSMC algorithm. Later, Lord extended the CL model even further to describe the scattering of diatomic molecules from a solid surface.<sup>11</sup>

Molecular dynamics (MD) simulations are considered as a powerful computational tool to study gas–solid interactions at the atomistic level. In fact, using MD simulations, it is possible to directly track individual molecules under a wide range of conditions and gain a detailed understanding of momentum and energy exchange mechanism at a gas–solid interface.<sup>17–20</sup> However, even with the help of fast computers it becomes very difficult to use a full MD approach for modeling gas–solid interactions in a physical system due to the huge computational costs.

Instead, recent approaches use the insight gained by the MD simulations to construct more elaborated GSI models inspired by the aforementioned empirical scattering models. Nevertheless, the performance of these models relies significantly on the values of the ACs used in these models, which act as calibration parameters. For instance, Yamamoto *et al.*<sup>13</sup> extended the Maxwell GSI model based on the MD simulation results for N<sub>2</sub>–Pt system. Assuming no dependency between translational velocity components, as well as the translational and rotational energy modes, they proposed using the tangential and normal momentum, and the translational and rotational energy ACs to reproduce corresponding velocity and energy components. The main drawback of the CLL model<sup>11</sup> is that the energy exchange between internal energy modes (e.g., the rotational energy mode) and the translational energy mode cannot be described by the model. To overcome this deficiency, Gorji and Jenny<sup>15</sup> extended the CLL model and proposed a new scattering model that could account for energy transfer between the internal and the translational energy modes. Based on the data obtained from the molecular beam experiment, they showed that energy exchange between different energy modes can happen at highly nonequilibrium situations. Using MD simulation data for calibration, they proposed a model with a relatively complex mathematical form, which resulted from coupling a fully diffuse and the CLL model, and depends on five different ACs.

In general, the accuracy of the empirical GSI models and their derivatives highly depends on the values of ACs, and this issue has been addressed as the main disadvantage of these models.<sup>21</sup> In fact, numerous parameters such as gas/solid materials, surface cleanliness and roughness, and gas/surface temperature can influence the obtained results for the ACs. Therefore, to measure the ACs,

accurately, all these parameters need to be controlled properly at atomistic level. This task is considered highly challenging either in an experimental study or MD simulation.<sup>22–24</sup>

In the case of rarefied gas flow systems with complex flow conditions that are far from thermal equilibrium, a vast range of physical phenomena could happen at the gas–solid interface that cannot be fully illustrated using a limited number of constant parameters. To overcome such deficiency, a new family of scattering kernels known as nonparametric scattering kernels has been introduced recently.<sup>25–27</sup> Generally, in these works as the first step based on the molecular beam setup, MD simulations have been carried out to study the interactions between a specific gas–solid combination. Afterward, based on the collisional data gathered from the MD simulations and without using any ACs as an intermediate parameter, a specific probability density function (PDF) estimation approach was employed to drive the probabilistic form of the scattering kernel.

Artificial intelligence and machine learning are other promising tools than can be employed to directly construct a probabilistic GSI model from the MD simulation data.<sup>28–30</sup> As an example, the Gaussian mixture (GM) approach, which is an unsupervised machine learning method, was used by Liao *et al.*<sup>28</sup> to construct a scattering kernel for monatomic gases based on the MD data obtained from the molecular beam simulation. In our previous work,<sup>29</sup> due to the crucial importance of the gas absorbed layer in the early transition regime ( $0.1 < Kn < 1$ ) on the energy and momentum transfer at gas/solid interface, instead of the molecular beam approach, we used a two-parallel wall MD setup as a reference system. We employed the GM model to construct a GSI model for monatomic gases. Comparison of the obtained results from the GM model against the CLL scattering model in different physical conditions proved the superiority of the GM model. Wu *et al.*<sup>30</sup> introduced a GM model for N<sub>2</sub>–Pt interactions using a molecular beam approach. Neglecting gas–gas interactions, they studied the effect of wall roughness on ACs and reflected velocity distributions. To the best of our knowledge, there is no GM-based scattering kernel for diatomic gases that, including gas–gas interactions, can deal with adsorption-related problems.

In this study, the GM model is used to construct a GSI model for diatomic gas molecule interactions with a given surface. Here, H<sub>2</sub> and N<sub>2</sub> gases are considered as the case studies, due to their numerous engineering applications, and very different molecular masses. At the first step, MD simulations have been carried out for H<sub>2</sub> and N<sub>2</sub> gases confined between Ni walls. Afterward, the pre- and postcollisional translational and rotational velocities of the gas molecules are utilized for the training the GM model. In doing so, the interplay between different velocity components, and the energy exchange between the translational and rotational energy modes that are likely to occur in nonequilibrium situations are implicitly taken into account in the model. The performance of the GM-based scattering model is examined against the CLL model in some important benchmark thermal problems such as the Fourier thermal problem, the Couette flow problem, and the combined Fourier–Couette flow problem. The examination is carried out in terms of various statistical and physical parameters.

## II. METHODOLOGIES

### A. MD simulation model

The MD simulation setup used in this work consisting of Ni walls in contact with H<sub>2</sub> or N<sub>2</sub> gas is presented in Fig. 1. Each Ni wall is

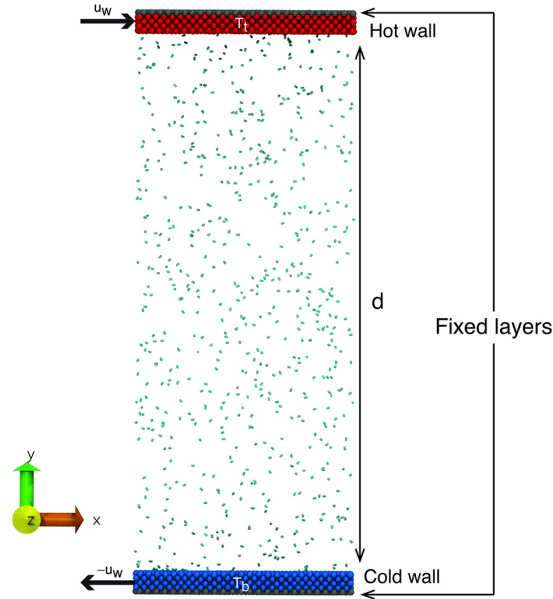


**FIG. 1.** Schematic representation of the simulation model;  $d$ : distance between the two walls;  $T_b$ : Temperature of the bottom wall;  $T_t$ : temperature of the bottom wall;  $u_w$ : prescribed velocity on the walls.

formed by five layers of FCC planes of solid Ni with a cross-sectional area of  $10.8 \times 10.8 \text{ nm}^2$ . The distance between the bottom and the top walls,  $d$ , is 30 nm. The outermost layer in each wall is kept fixed in order to prevent the translational movement of the walls in the  $y$ -direction. Diatomic gas molecules are considered as rigid rotors with a fixed bond length of 0.7414 and 1.097 Å for  $\text{H}_2$  and  $\text{N}_2$ , respectively.<sup>31</sup> The total number of gas molecules confined between the two Ni walls is decided in such a way that the mean free path,  $\lambda$ , of gas molecules remains around 10.5 nm, which results in the Knudsen number of  $Kn = 0.35$  for both systems.

Periodic boundary conditions are applied along  $x$  and  $z$  directions. The embedded atom model (EAM) potential<sup>32</sup> is employed to model the interactions between Ni atoms. The non-bonded interactions between gas-gas and gas-wall atoms are modeled using COMPASS force field,<sup>33</sup> in which a Lennard-Jones (L-J) 9-6 function is employed to describe the interactions. For two atoms of the same kind, the potential parameters ( $\epsilon_{ii}$ ,  $\sigma_{ii}$ ) can be found in the COMPASS database.<sup>34</sup> However, for a mixture of two different atoms, the potential parameters are calculated using the sixth-power Waldman-Hagler combining rules<sup>35</sup>

$$\epsilon_{ij} = 2\sqrt{\epsilon_{ii}\epsilon_{jj}} \left[ \frac{\sigma_{ii}^3 \cdot \sigma_{jj}^3}{\sigma_{ii}^6 + \sigma_{jj}^6} \right], \quad (1)$$

$$\sigma_{ij} = \left[ \frac{\sigma_{ii}^6 + \sigma_{jj}^6}{2} \right]^{\frac{1}{6}}. \quad (2)$$

All the gas-gas and gas-wall interatomic potential parameters used in this study are listed in Table I. The cutoff distance for gas-gas and gas-wall interactions is set at  $2.5\sigma_{ii}$  and 10 Å, respectively.

In the first step, for each MD simulation setup, the energy minimization is performed by iteratively adjusting atom positions. In the

**TABLE I.** Lennard-Jones potential parameters.

Atom pair	$\epsilon$ (eV)	$\sigma$ (Å)
Ni-Ni <sup>38</sup>	$6.6 \times 10^{-1}$	2.239
H-H	$9.29 \times 10^{-4}$	1.421
H-Ni	$1.19 \times 10^{-2}$	2.016
N-N	$2.57 \times 10^{-3}$	3.8
N-Ni	$1.61 \times 10^{-2}$	3.408

next step, each wall is equilibrated at the desired temperature level using Nose-Hoover thermostat<sup>36</sup> (NVT), while gas molecules are modeled in the microcanonical ensemble (NVE), and their temperature can only change by exchanging kinetic energy with other molecules in the simulation box via collisions. However, in order to accelerate the equilibration process, the velocity components of gas molecules are initially sampled from a Gaussian distribution with a mean value of 0.0 and a standard deviation of  $\sqrt{\frac{k_B T_a}{2m_g}}$ , where  $T_a$  is the average value of the bottom and top wall temperatures, and  $m_g$  is the mass of gas molecule.

To model the Couette flow condition, as it is depicted in Fig. 1, the top wall moves with the velocity  $u_w$ , whereas the bottom wall has the velocity  $-u_w$ . Herein, the speed ratio  $S_v$  is assigned as

$$S_v = \frac{u_w}{\sqrt{2k_B T_b / m_g}}, \quad (3)$$

where  $T_b$  is the temperature of the bottom wall. In order to attain the desired  $\lambda$  and  $Kn$  in the systems, all simulation setups are equilibrated for 3 ns to reach the required temperature and pressure with a time step of 0.5 and 1.0 fs for  $\text{H}_2$ -Ni and  $\text{N}_2$ -Ni systems, respectively. Afterward, the production run is followed, which is carried on for 25 ns for  $\text{H}_2$ -Ni system and 60 ns for  $\text{N}_2$ -Ni system. All MD simulations are conducted using LAMMPS<sup>37</sup> package.

## B. Scattering kernel

In the transitional flow regime ( $0.1 < Kn < 10$ ), the Boltzmann equation must be employed as the governing equation to solve the problems of gas flows. Having a precise and detailed understating of boundary conditions is crucial in order to guarantee the reliability of the simulation results, while considering flows of gas around bodies or adjacent to a solid surface. The boundary condition defines the relation between the incoming and outgoing gas molecular velocity distributions,  $f(\mathbf{v}')$  and  $f(\mathbf{v})$ , at the boundary surface. It can be represented generally through the scattering kernel  $R(\mathbf{v}|\mathbf{v}')$  as

$$v_n f(\mathbf{v}) = \int_{v'_n < 0} |v'_n| R(\mathbf{v}|\mathbf{v}') f(\mathbf{v}') d\mathbf{v}', \quad v_n > 0. \quad (4)$$

Here,  $\mathbf{v}'$  and  $\mathbf{v}$  are the translational velocities of the center of mass (COM) for the incoming and outgoing molecules, respectively. The velocities  $v_n$  and  $v'_n$  are the corresponding normal components of the molecular velocities directed into the gas domain and normal to the surface. The scattering kernel  $R(\mathbf{v}|\mathbf{v}')$  denotes the probability that a stream of incoming gas molecules with velocity in  $[\mathbf{v}', \mathbf{v}' + d\mathbf{v}']$  will be bounced off with a new velocity in the interval of  $[\mathbf{v}, \mathbf{v} + d\mathbf{v}]$ .

However, in the case of a diatomic gas molecule, in addition to the translational velocity components, the rotational velocity vectors ( $\omega'$ ,  $\omega$ ) need to be taken into account, as well. Therefore, the scattering kernel must be substituted by  $R(\mathbf{v}, \omega | \mathbf{v}', \omega')$  and the probability density must be substituted by  $f(\mathbf{v}, \omega)$ . The CLL model is the most accurate empirical scattering kernel that commonly used in diatomic rarefied gas flow simulations, and it is given in the following form:<sup>11</sup>

$$R^{CLL}(\mathbf{v}, \omega | \mathbf{v}', \omega') = \frac{2v_n}{\pi^2 \alpha_t (2 - \alpha_t) \alpha_n \alpha_{rot}} \exp \left[ -\frac{[\mathbf{v}_t - \sqrt{1 - \alpha_t} \mathbf{v}'_t]^2}{\alpha_t (2 - \alpha_t)} \right] \times \exp \left[ -\frac{v_n^2 + (1 - \alpha_n) v_n'^2}{\alpha_n} \right] I_0 \left[ \frac{2(\sqrt{1 - \alpha_n}) v_n v_n'}{\alpha_n} \right] \times \exp \left[ -\frac{(\omega - \sqrt{1 - \alpha_{rot}} \omega')^2}{\alpha_{rot}} \right], \quad (5)$$

where  $\alpha_t$ ,  $\alpha_n$ , and  $\alpha_{rot}$  are the accommodation coefficients corresponding to the tangential momentum, normal translational kinetic energy, and rotational energy, respectively.  $\mathbf{v}_t$  represents the tangential velocity vector, and  $I_0$  is the modified Bessel function of the first kind and zeroth order. The translational ( $\mathbf{v}'$ ,  $\mathbf{v}$ ) and rotational ( $\omega'$ ,  $\omega$ ) velocity vectors are normalized by  $\sqrt{\frac{2k_B T_w}{m_g}}$  and  $\sqrt{\frac{2k_B T_w}{I}}$ , respectively. Here,  $T_w$  describes the wall temperature and  $I$  is the mass moment of inertia of the diatomic gas molecule. The algorithm and formulas used in this work to generate post-collisional velocities according to the CLL scattering kernel are given in Ref. 15. The required accommodation coefficients in Eq. (5) are calculated using the proposed method in Ref. 17, which is based on the least squares approximation on the collisional data containing impinging  $\Phi_I$  and reflected  $\Phi_R$  quantities

$$\alpha_\phi = 1 - \frac{\sum_i (\Phi_I^i - \langle \Phi_I \rangle) (\Phi_R^i - \langle \Phi_R \rangle)}{\sum_i (\Phi_I^i - \langle \Phi_I \rangle)^2}, \quad (6)$$

where  $\phi$  can be related to the different kinetic properties of the gas molecules such as its center of mass velocity in a certain direction, as well as its translational  $E_{tr} = \frac{1}{2} m_g v^2$ , rotational  $E_{rot} = \frac{1}{2} I \omega^2$ , or total  $E_{tot} = E_{tr} + E_{rot}$  kinetic energy. Collisions are tracked by defining a virtual plane at a distance of one gas-wall interaction cutoff radius away from the walls ( $r_{plane} = r_{cutoff} = 10 \text{ \AA}$ ). Collisional data are recorded when the geometric center of mass of the molecule crosses the virtual plane. The final datasets gathered from MD simulations of different systems include between 100 000 and 150 000 data points.

### C. Gaussian mixture model

Gaussian mixture (GM) model is a probabilistic clustering approach for illustrating normally distributed subset within an overall dataset. The GM model typically does not require knowing from which subset a data point comes, and the model learns the subsets automatically. Having this feature, the GM model is identified as an unsupervised machine learning technique. Due to its robustness and flexibility, the GM model has been utilized in a wide variety of important practical situations such as language identification, anomaly

detection, pattern recognition, signal processing, and object tracking of multiple objects.<sup>39–42</sup>

In the GM model, a superposition of  $M$ -dimensional Gaussian functions is employed to estimate the probability density function of data  $\mathbf{X}$  as

$$p(\mathbf{X}) = \sum_{i=1}^K \rho_i N(\mathbf{X} | \bar{\mu}_i, \Sigma_i), \quad (7)$$

where  $K$  is the number of Gaussians.  $\rho_i$ ,  $i = 1, 2, \dots, K$  are the mixture component weights with the constraint that  $\sum_{i=1}^K \rho_i = 1$ ,  $\bar{\mu}_i$  is the mean vector, and  $\Sigma_i$  is the covariance matrix.  $N(\mathbf{X} | \bar{\mu}_i, \Sigma_i)$  are the components density functions, which are indeed  $M$ -dimensional normal distributions given by

$$N(\mathbf{X} | \bar{\mu}_i, \Sigma_i) = \frac{1}{(2\pi)^{M/2} |\Sigma_i|^{1/2}} \exp \left[ -\frac{1}{2} (\mathbf{X} - \bar{\mu}_i)' \Sigma_i^{-1} (\mathbf{X} - \bar{\mu}_i) \right]. \quad (8)$$

The model parameters ( $\psi = \{\rho_i, \bar{\mu}_i, \Sigma_i\} \forall i \in \{1 \dots K\}$ ) are determined using the expectation-maximization (EM) optimization algorithm.<sup>43</sup> However, before implementing the EM algorithm to estimate the GM model parameters, it is essential to define the model attributes such as the type of covariance matrix<sup>28</sup> (e.g., spherical, diagonal, tied, or full) and the number of Gaussians. In this work, the full covariance matrix has been applied that has the best performance, and it is taken as the default covariance matrix in the SCIKIT-LEARN<sup>44</sup> package used to implement the GM model. The number of Gaussians is a crucial parameter that is required to be specified adequately by the user to avoid underfitting or overfitting in the model, and it directly affects the accuracy and the computational cost of the model. To determine the optimal  $K$ , a sensitivity analysis has been carried out. It is discussed in detail in Appendix A. From this analysis, in this work,  $K = 500$  and  $K = 450$  are used as the number of Gaussians for  $\text{H}_2$ -Ni and  $\text{N}_2$ -Ni systems, respectively.

The collisional data used to train the GM model are a ten-dimensional dataset including impinging and outgoing translational velocities of the COM of the molecules ( $v'_x, v'_y, v'_z, v_x, v_y, v_z$ ), as well as impinging and outgoing rotational velocities of the molecules ( $\omega'_1, \omega'_2, \omega_1, \omega_2$ ). Including both translational and rotational degrees of freedom for training purpose indicates that the possible energy transfer between translational and rotational modes in the case of non-equilibrium condition is taken into account in this model. From each dataset obtained from a specific MD simulation, 75% of the trajectories (consisting of translational and rotational velocities), along with a desired number of Gaussians, are fed into the GM model for training. The remaining data are used for validation purpose.

Here, except the normal velocity components ( $v'_y, v_y$ ) that follow a Rayleigh distribution, the other velocity components follow a Gaussian distribution. As it has been comprehensively discussed in our previous work,<sup>29</sup> the GM model performs better when all the components of the original MD data have Gaussian distributions. Therefore, exploiting the preprocessing scheme proposed by Liao *et al.*,<sup>28</sup> the normal velocity components have been transferred from Rayleigh to Gaussian distributions. First, for each normal velocity pair ( $v'_y, v_y$ ), its equivalent inverse ( $-v'_y, -v_y$ ) is added to the dataset.

Second, using the following scheme [Eq. (9)] the distributions of the normal velocity components are transferred from Rayleigh to Gaussian:

$$T(\theta) = \sqrt{2\beta} \operatorname{erf}^{-1} \left[ 1 - 2 \exp \left( -\frac{\theta^2}{2\beta} \right) \right], \quad \beta = \frac{k_B T_g}{m_g}, \quad (9)$$

where  $T_g$  refers to the gas temperature and can be computed using the average translational kinetic energy of the gas. The first step of preprocessing scheme doubles the size of velocity data in the normal direction. Therefore, half of the final obtained data is chosen and used for training alongside with the other components in the dataset. In accordance with the distribution of the final data used for training the GM model, the obtained velocities from the model also have Gaussian distribution. Hence, to compare the model predictions with the initial MD results, the predicted velocity components in the normal direction are transformed back into the Rayleigh distribution as follows:

$$Z(\theta) = \sqrt{-2\beta \ln \left[ \frac{1}{2} - \frac{1}{2} \operatorname{erf} \left( \frac{\theta}{\sqrt{2\beta}} \right) \right]}. \quad (10)$$

### III. RESULTS AND DISCUSSION

This section is divided into three main parts. The first part is devoted to validate the MD simulation approach used in this work to study the diatomic gas–solid surface interactions. In the second part, the performance of the GM and CLL scattering models in three thermal problems, commonly encountered in rarefied gas flow systems, is investigated. Finally, in the last part based on the density profiles extracted from the MD simulations, the reasons for different behaviors of  $H_2$  and  $N_2$  gases in terms of thermal behaviors and flow properties are discussed.

#### A. MD scheme validation

Using experimental results, our aim is to validate first the force fields used in the simulations and second to prove the suitable methods to extract ACs from MD data. Here, the tangential momentum accommodation coefficient ( $\alpha_x$ ) and the total thermal energy accommodation coefficient ( $\alpha_{tot}$ ) for  $H_2$ –Ni and  $N_2$ –Ni systems obtained from the MD simulations are compared with the corresponding experimental values in the literature. For this, we replicated the experimental conditions using a two-parallel plate setup<sup>45</sup> ( $T_b = 288$  K,  $T_t = 308$  K,  $S_v = 0$ ) in the MD simulations.

From MD simulations for  $H_2$ –Ni system, the values of  $\alpha_x$  and  $\alpha_{tot}$  computed on the bottom wall were 0.953 and 0.316, respectively. With regard to  $\alpha_x$ , no measurement on Ni surface was found in the literature. Knowing that surface material has minor impact on the value of  $\alpha_x$ ,<sup>46</sup> the results on the other metal surfaces have been used for the comparison purpose. Herein, the reported experimental value of  $\alpha_x$  for  $H_2$  on Bronze surface is 0.94,<sup>23</sup> which is consistent with the value computed in this work. In addition to that, for  $H_2$ –Ni, an empirical study showed that  $\alpha_{tot} = 0.293$ ,<sup>47</sup> which is in good agreement with the MD obtained value.

In the case of  $N_2$ –Ni, the results obtained from MD simulations are  $\alpha_x = 0.87$  and  $\alpha_{tot} = 0.869$ . The reported values for  $\alpha_x$  on different surfaces are in the range of  $0.84 < \alpha_x < 1$ .<sup>46</sup> Referring to  $\alpha_{tot}$ , the value reported by Amdur *et al.*<sup>47</sup> for  $N_2$ –Ni is 0.823, which is consistent with the value computed in this work. Based on the presented results, it can be deduced that the choice of the intermolecular potentials and the

atomic schemes to study GSIs in this work are quite reliable for studying further the three thermal problems we want to investigate.

#### B. GM model Assessment

Using the MD simulation results for  $H_2$ –Ni and  $N_2$ –Ni as the reference solutions, we aim to assess the performance of the GM and CLL scattering models in predicting the gas velocities after the collision with the solid walls.

Three different benchmark problems, namely, the Fourier thermal problem, the Couette flow problem, and the combined Fourier–Couette flow problem, are examined. In the case of the Fourier thermal problem, the bottom wall has the temperature  $T_b = 300$  K, while the temperature of the top wall is  $T_t = 300$  K (named the isothermal walls system) or 500 K (named non-isothermal walls system). For the Couette flow problem, the considered velocity ratios are  $S_v = 0.2$  or 0.4, and both walls have the same temperatures  $T_b = T_t = 300$  K. For the combined Fourier–Couette flow problem, using the non-isothermal wall system as the initial system, different velocity ratios ( $S_v = 0.2$  or 0.4) are imposed on the walls. The training of the GM model in each case study is carried out separately. For each case study, the most significant results are addressed in the main text, while the remaining ones for  $H_2$ –Ni and  $N_2$ –Ni can be found in [Appendixes B and C](#), respectively.

To generate the outgoing velocities based on the CLL model, first of all, the required ACs including TMAC in  $x$  and  $z$  directions ( $\alpha_x, \alpha_z$ ),  $\alpha_m$  and  $\alpha_{rot}$  are computed using the collected MD collisional data from each specific case study. Afterward, the post-collisional velocities are generated by using the computed ACs according to the method described in Ref. 15. In the case of the systems with moving walls, the value of the imposed velocity at the wall ( $u_w$ ) is added to the all velocity components generated by the CLL model in the direction of wall movement ( $V_{x,final} = V_{x,CLL} + u_w$ ).

The evaluation of the aforementioned stochastic GSI models has been carried out in terms of the correlation between the incoming and outgoing translational velocity components of COM ( $V_x, V_y, V_z$ ), different energy modes of the gas molecules ( $E_{tr}, E_{rot}, E_{tot}$ ), as well as the PDF of the outgoing velocity components or the energy modes. To compare the resulted PDFs in a quantitative manner, the Kullback–Leibler divergence (KLD)<sup>48</sup> also known as information divergence or relative entropy is employed. KLD, as the most commonly used information criterion for evaluating the model discrepancy, is being used frequently in machine learning studies to measure the difference between the actual and observed or predicted probability distributions. Suppose  $p(x)$  and  $q(x)$  are two PDFs on the same probability space  $\chi$ , the KLD is defined as

$$KLD(p(x)||q(x)) = \sum_{x \in \chi} p(x) \ln \frac{p(x)}{q(x)} dx, \quad (11)$$

where  $x$  can be referred to the velocity or energy data obtained from either MD simulations or GSI models. To calculate  $p(x)$  and  $q(x)$ , the related data space is evenly segmented into  $n$  bins. The density in each bin is computed by counting the number of samples in the bin. In addition to the correlations and PDFs, the corresponding ACs for the aforementioned kinetic features of the gas molecules have been used for the assessment purpose.

All the aforementioned properties are tested because, as it will be shown in Sec. III B 1, in some case studies even if PDFs or ACs are in agreement, velocity correlations can be different affecting the heat transfer predictions.

### 1. $H_2$ -Ni system

The velocity and energy distributions determined by the atomistic simulations and different GSI models for the isothermal Fourier thermal problem are plotted in Fig. 2. It is seen that in this case study, which resembles the fully equilibrium situation in the system, there is a perfect match between the correlation plots and PDFs of the partial translational velocity components, and the rotational energy mode. However,  $E_{tr}$  clouds of the MD simulation and the GM model are slightly narrower than the CLL model. Since  $E_{tot} = E_{tr} + E_{rot}$ , this mismatch is propagated into the  $E_{tot}$  cloud, as well. This issue can be also deduced from the values of the ACs in Table II, in which

**TABLE II.** Tangential momentum ( $\alpha_x, \alpha_z$ ), normal momentum ( $\alpha_y$ ), translational ( $\alpha_{tr}$ ), rotational ( $\alpha_{rot}$ ), and total ( $\alpha_{tot}$ ) energy accommodation coefficients of the Fourier thermal problem for  $H_2$ -Ni system ( $T_b = 300$  K), computed using different scattering kernels: GM and CLL models, and MD simulations. B: bottom wall; T: top wall.

$T_t$	Model	Wall	$\alpha_x$	$\alpha_y$	$\alpha_z$	$\alpha_{tr}$	$\alpha_{rot}$	$\alpha_{tot}$
300	MD	B	0.958	0.797	0.955	0.526	0.666	0.326
	GM	B	0.958	0.798	0.954	0.558	0.700	0.379
	CLL	B	0.959	0.783	0.955	0.880	0.666	0.810
500	MD	B	0.928	0.748	0.820	0.452	0.600	0.234
		T	0.923	0.777	0.924	0.473	0.600	0.274
	GM	B	0.927	0.747	0.933	0.481	0.634	0.296
		T	0.921	0.776	0.922	0.507	0.636	0.340
	CLL	B	0.929	0.713	0.930	0.859	0.601	0.776
		T	0.922	0.774	0.926	0.864	0.595	0.775

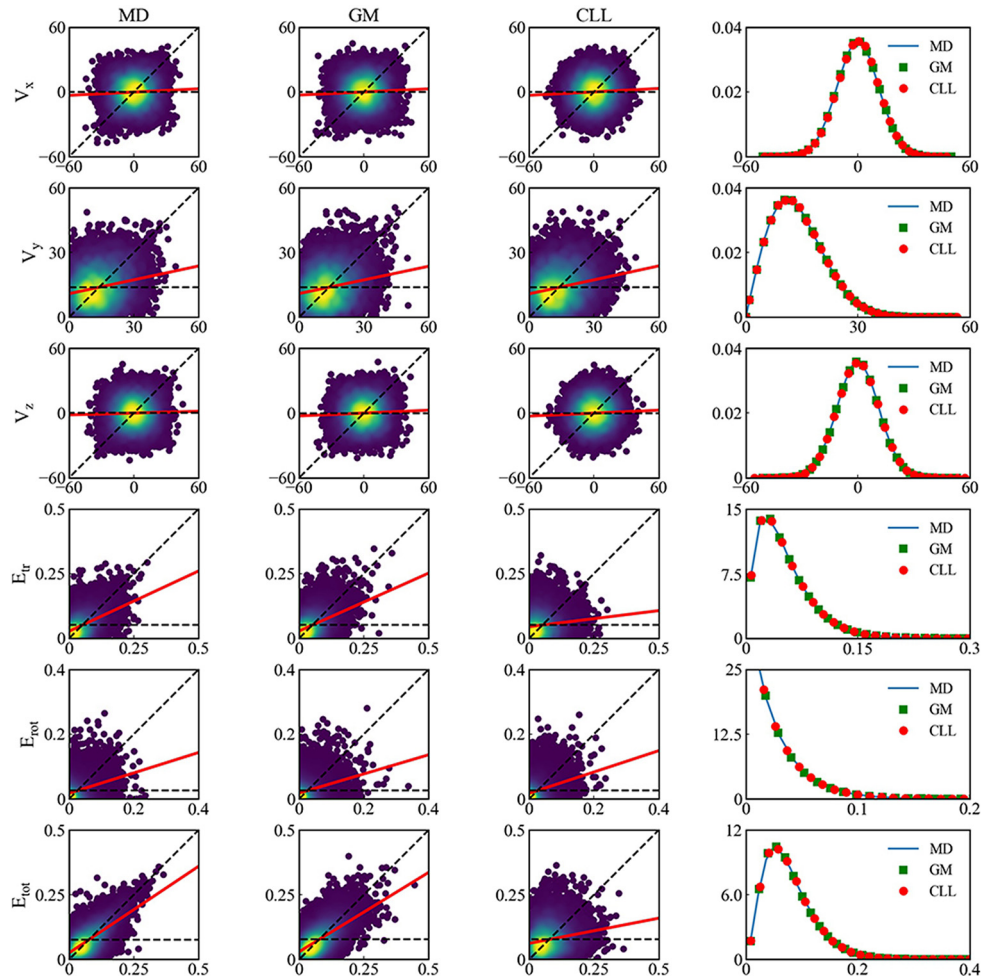


**FIG. 2.** Correlations between incoming (horizontal-axis) and outgoing (vertical-axis) translational velocity components in ( $\text{\AA}/\text{ps}$ ) and energy modes in (eV) of the isothermal Fourier thermal problem for  $H_2$ -Ni system at the bottom wall. The dashed horizontal and diagonal lines demonstrate fully diffusive and specular reflection, respectively. Solid red lines demonstrate the least-square linear fit of the kinetic data. In the last column, the corresponding probability density functions of translational velocity components and energy modes for the reflecting particles are presented.



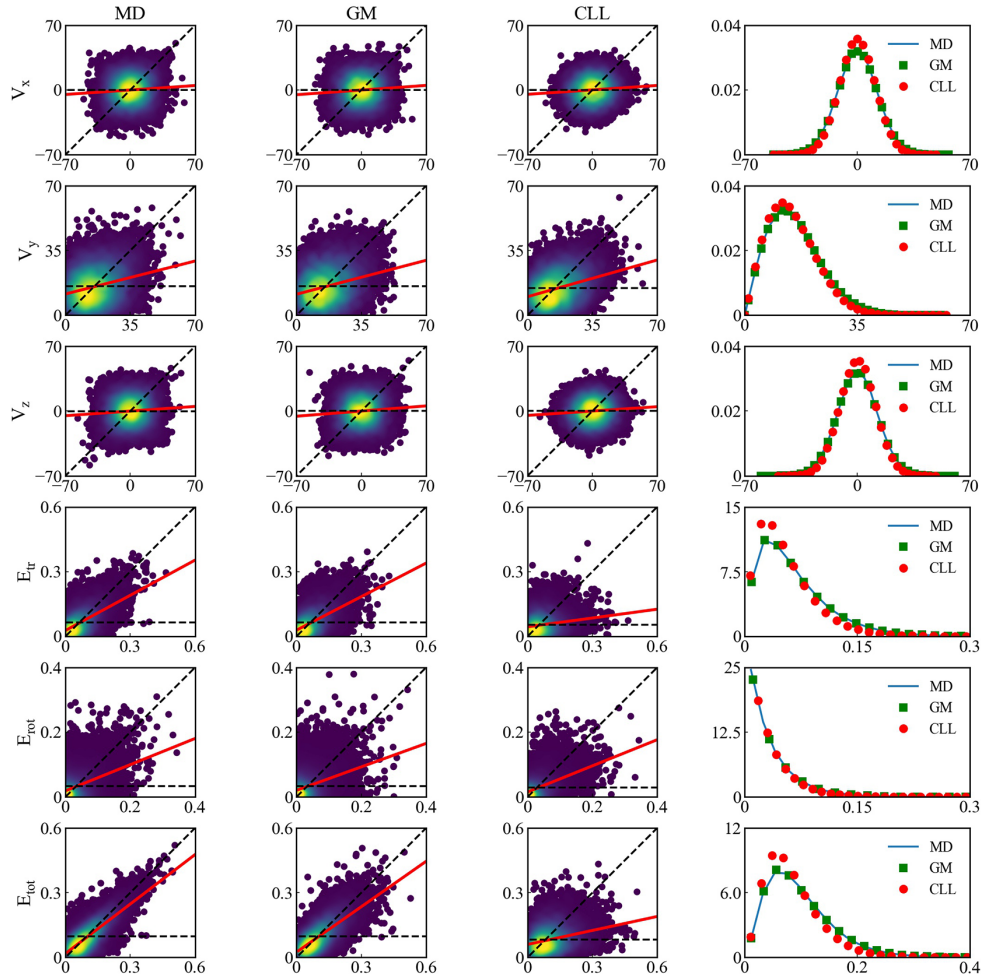


**FIG. 3.** Correlations between incoming (horizontal-axis) and outgoing (vertical-axis) translational velocity components in (Å/ps) and energy modes in (eV) of the non-isothermal Fourier thermal problem for H<sub>2</sub>-Ni system at the bottom wall. The dashed horizontal and diagonal lines demonstrate fully diffusive and specular reflection, respectively. Solid red lines demonstrate the least-square linear fit of the kinetic data. In the last column, the corresponding probability density functions of the translational velocity components and energy modes for the reflecting particles are presented.

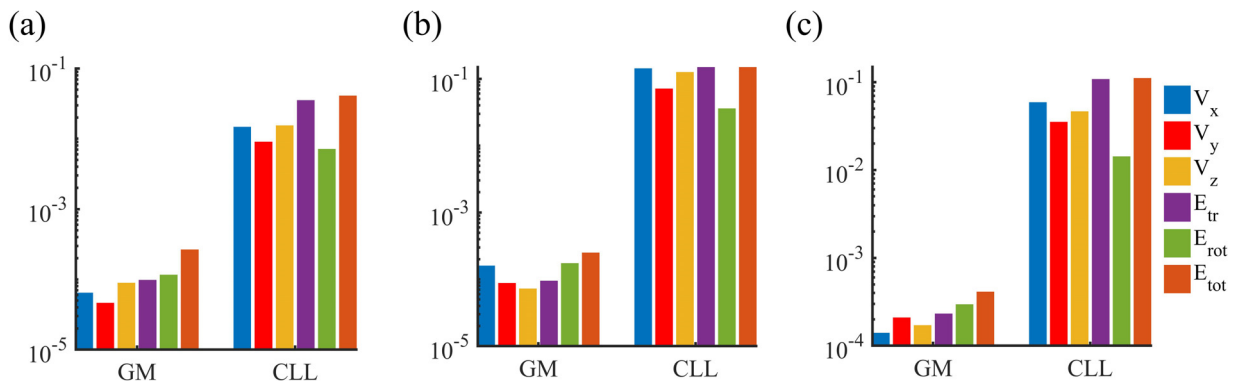


**FIG. 4.** The Kullback-Leibler divergence of the translational velocity components and different energy modes of H<sub>2</sub>-Ni system determined by GM and CLL scattering models; (a) non-isothermal Fourier thermal problem at the bottom wall; (b) Couette flow problem ( $S_y = 0.4$ ) at the bottom wall; (c) combined Fourier-Couette flow problem ( $S_y = 0.4$ ) at the top wall.

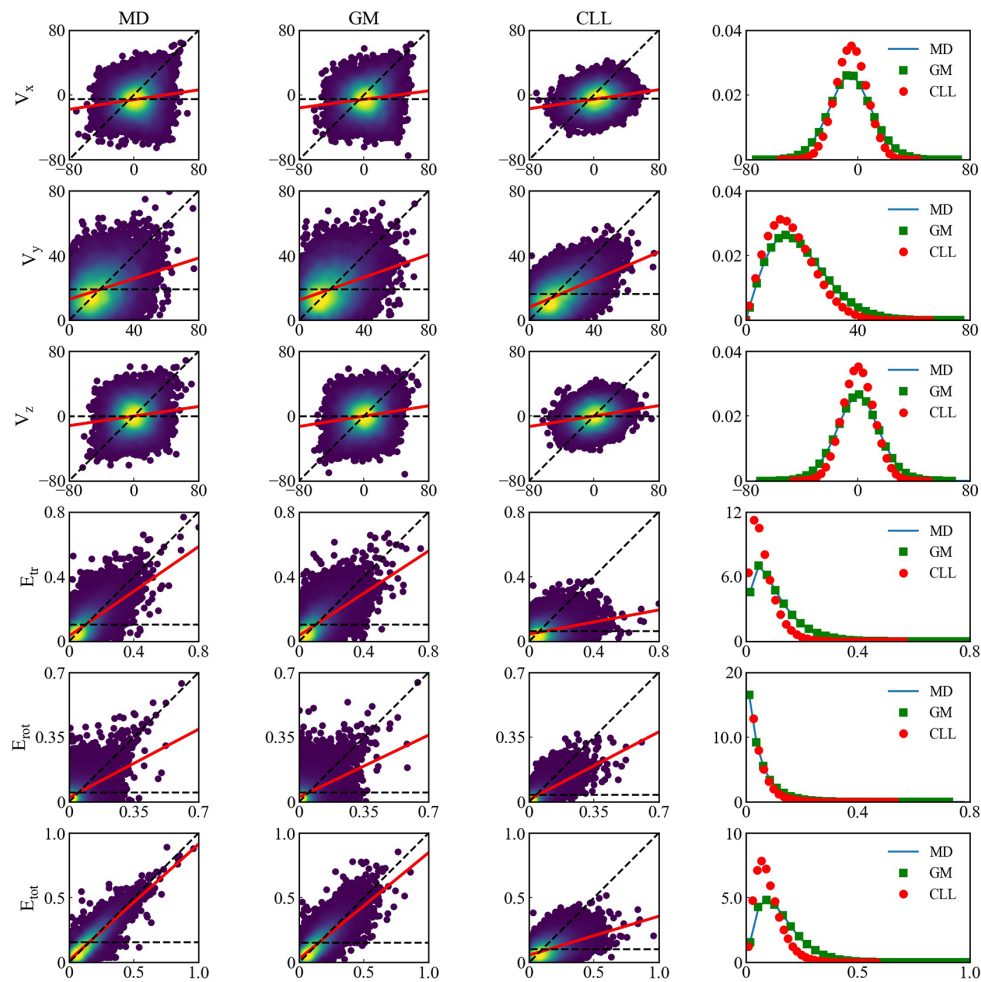


**FIG. 5.** Correlations between incoming (horizontal-axis) and outgoing (vertical-axis) translational velocity components in ( $\text{\AA}/\text{ps}$ ) and energy modes in (eV) of Couette flow problem ( $S_v = 0.4$ ) for  $\text{H}_2$ -Ni system at the bottom wall. The dashed horizontal and diagonal lines demonstrate fully diffusive and specular reflection, respectively. Solid red lines demonstrate the least-square linear fit of the kinetic data. In the last column, the corresponding probability density functions of the translational velocity components and energy modes for the reflecting particles are presented.

various ACs of the Fourier thermal problem for the  $\text{H}_2$ -Ni system are presented. It is observed that there is a perfect match between the values of  $\alpha_x$ ,  $\alpha_y$ ,  $\alpha_z$ , and  $\alpha_{rot}$  obtained from the GM and CLL scattering models with the MD simulations, while the values of  $\alpha_{tr}$  and  $\alpha_{tot}$  obtained from the wall scattering models are larger than the values obtained directly from the MD simulations. However, in comparison with CLL results, the values obtained from the GM scattering model are much closer to the MD results.

The correlation plots and the PDFs at the bottom wall of the non-isothermal Fourier thermal system are shown in Fig. 3. While the correlation plots acquired from the GSI models for the translational velocity components are in good agreement with the MD simulation results, a deviation is observed around the peak values in the PDFs obtained from the CLL model (e.g., see the PDF of  $E_{tr}$  in Fig. 3). Since the peak value in such distributions provides a measure of temperature, predicting higher peaks by the CLL model implies that gas molecules accommodate more to the surface, and this leads to a lower

temperature for the reflected gas molecules. The predicted outgoing translational velocities by the statistical GSI models and the original MD results were employed to compute the temperature of the gas after colliding with the surface. The postcollisional gas temperature according to the MD results and the GM model was 377.51 and 374.23 K, respectively. However, the CLL model gave the outgoing temperature of 315.1 K. This underprediction of the temperature confirms the aforementioned statement. With regard to the various energy modes of the gas molecules, the results from the GM model are always in a reasonable agreement with the MD simulation results. However, the correlation plots and the PDFs obtained based on the CLL model for  $E_{tr}$  and  $E_{tot}$  deviate from the MD results, which predict the reflection in a more diffuse manner according to the CLL model. On the contrary, the predicted  $E_{rot}$  by the CLL model matches well with the MD data, although looking to the correlation plots, the MD data are more dispersed than the CLL scattering model results. Based on the predicted translational velocity components and the energy modes by the GM

**TABLE III.** Tangential momentum ( $\alpha_x, \alpha_z$ ), normal momentum ( $\alpha_y$ ), translational ( $\alpha_{tr}$ ), rotational ( $\alpha_{rot}$ ), and total ( $\alpha_{tot}$ ) energy accommodation coefficients of the Couette flow problem for  $H_2$ -Ni system at different speed ratios ( $S_v$ ), computed using different scattering kernels: GM and CLL models, and MD simulations.

$S_v$	Model	$\alpha_x$	$\alpha_y$	$\alpha_z$	$\alpha_{tr}$	$\alpha_{rot}$	$\alpha_{tot}$
0.2	MD	0.942	0.743	0.933	0.432	0.610	0.220
	GM	0.940	0.742	0.931	0.466	0.651	0.284
	CLL	0.941	0.713	0.932	0.855	0.615	0.777
0.4	MD	0.854	0.655	0.846	0.307	0.477	0.105
	GM	0.853	0.660	0.844	0.351	0.526	0.183
	CLL	0.854	0.570	0.845	0.809	0.477	0.700

and CLL GSI models, the KLD coefficient between these models and the original MD results were computed [see Fig. 4(a)]. It is seen that the deviation between the CLL model and the MD results is 2 orders of

magnitudes larger than the deviation between the GM model and MD results. By looking at the reported ACs of this case study (see Table II), it is inferred that similar to the previous case study, the results from the GM model in comparison with the CLL model are overall in a better agreement with the MD simulation results. Comparing the values of the ACs in this case study with the isothermal Fourier problem, it is noted that all the computed ACs are slightly lower. This is in line with the previously observed trend of decreasing AC by increased kinetic energy of the gas molecules<sup>49,50</sup> that in this case study is caused by having higher temperature at the top wall.

Figure 5 shows the scattering results based on the MD simulations and the employed stochastic GSI model for the Couette flow problem with  $S_v = 0.4$ . It is seen that the GM model results are in good agreement with the MD simulation results. However, in the case of the CLL model, except for the rotational energy, the other energy modes ( $E_{tr}$ ,  $E_{tot}$ ), as well as the partial velocity components ( $V_x$ ,  $V_y$ ,  $V_z$ ), significantly deviate from the MD results. For the tangential

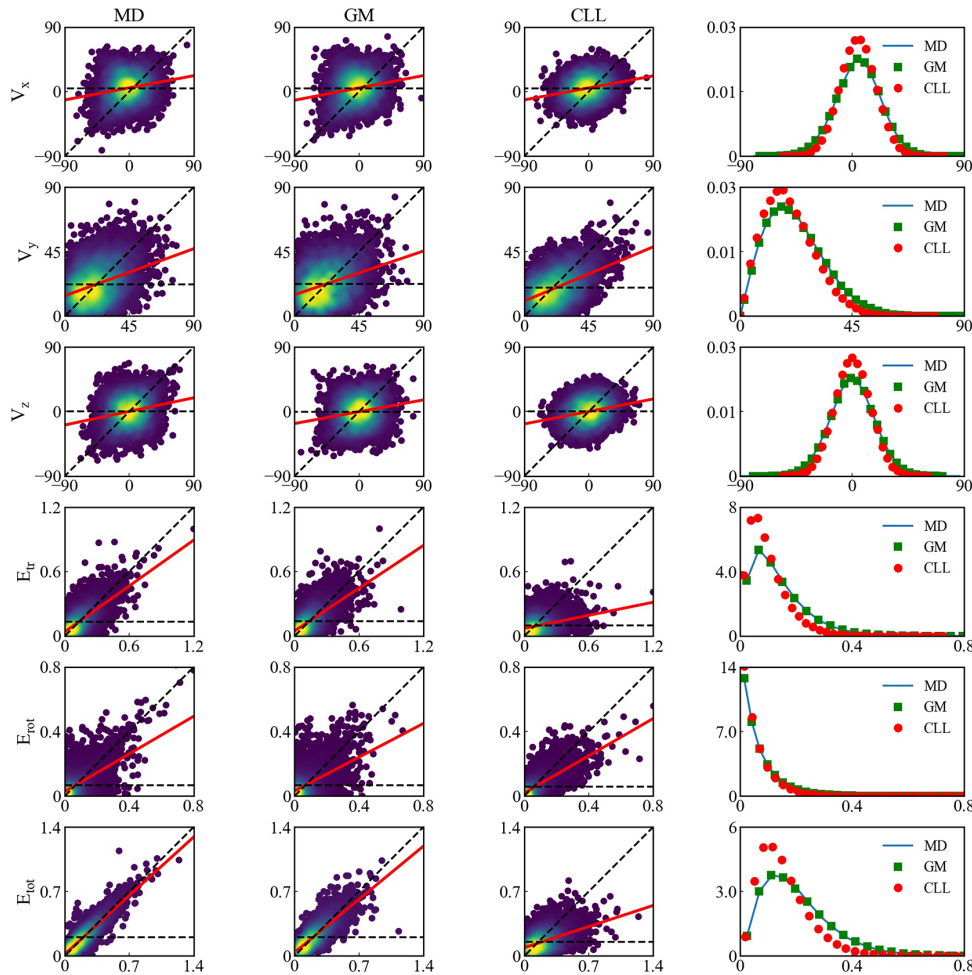


**FIG. 6.** Correlations between incoming (horizontal-axis) and outgoing (vertical-axis) translational velocity components in ( $\text{\AA}/\text{ps}$ ) and energy modes in (eV) of the combined Fourier-Couette flow problem for  $H_2$ -Ni system at the top wall ( $S_v = 0.4$ ). The dashed horizontal and diagonal lines demonstrate fully diffusive and specular reflection, respectively. Solid red lines demonstrate the least-square linear fit of the kinetic data. In the last column, the corresponding probability density functions of the translational velocity components and energy modes for the reflecting particles are presented.

**TABLE IV.** Tangential momentum ( $\alpha_x, \alpha_z$ ), normal momentum ( $\alpha_y$ ), translational ( $\alpha_{tr}$ ), rotational ( $\alpha_{rot}$ ), and total ( $\alpha_{tot}$ ) energy accommodation coefficients of the combined Fourier–Couette flow problem for  $H_2$ –Ni system at different speed ratios ( $S_v$ ), computed using different scattering kernels: GM and CLL models, and MD simulations. B: bottom wall; T: top wall.

$S_v$	Model	Wall	$\alpha_x$	$\alpha_y$	$\alpha_z$	$\alpha_{tr}$	$\alpha_{rot}$	$\alpha_{tot}$
0.2	MD	B	0.913	0.705	0.904	0.379	0.544	0.155
		T	0.913	0.726	0.896	0.397	0.556	0.190
	GM	B	0.912	0.709	0.908	0.421	0.593	0.232
		T	0.916	0.726	0.892	0.435	0.590	0.259
	CLL	B	0.913	0.647	0.904	0.831	0.544	0.738
		T	0.908	0.718	0.893	0.838	0.559	0.745
0.4	MD	B	0.812	0.633	0.801	0.274	0.418	0.075
		T	0.808	0.646	0.805	0.286	0.420	0.092
	GM	B	0.807	0.633	0.802	0.314	0.479	0.155
		T	0.813	0.649	0.807	0.328	0.480	0.167
	CLL	B	0.812	0.527	0.800	0.791	0.419	0.667
		T	0.808	0.591	0.804	0.796	0.420	0.670

velocity components, the obtained ACs are similar. This can be understood by comparing the slope of the red lines in the correlation graphs obtained from the MD simulations and the scattering models in the tangential directions, as well as the values of  $\alpha_x$  and  $\alpha_z$  reported in Table III. However, the shape of the resulted velocity clouds obtained from the CLL model is different from the ones resulted from the original MD data and the GM model. In both tangential directions, the CLL results have ellipsoidal shapes and look symmetrical around the horizontal dashed line. However, MD simulation correlation graphs in the tangential directions are more concentrated around the diagonal lines. In fact, MD results show that in case the magnitude of the incoming velocity is large, there is a strong correlation between incoming and outgoing velocities. This causes that the velocity clouds become narrower in their ending points around the diagonal line at high velocities (see Fig. 5). Comparison of the tangential velocity clouds from the employed GSI models with the MD results indicates that the aforementioned behavior can be captured by the GM model, and not by the CLL model.

KLDs based on the obtained scattering results in this case study are shown in Fig. 4(b). Comparing the GM results with the non-isothermal Fourier system [see Fig. 4(a)], the most noticeable difference is a higher KLD value for  $V_x$  component in the current case study (2.5 times higher), indicating relatively poor performance of the GM model here. However, the deviation of the CLL model and the MD results are much more noticeable in this case study. The ACs obtained from MD simulations, and different GSI models for the Couette flow problem are reported in Table III. It is seen that  $\alpha_x, \alpha_y,$  and  $\alpha_z$  obtained from both scattering models agree well with the MD simulation results. With regard to the energy ACs,  $\alpha_{rot}$  obtained from the CLL model has a slightly better match with MD results than the value obtained from the GM. However, while the values of  $\alpha_{tr}$  and  $\alpha_{tot}$  obtained from CLL are significantly larger than the MD results, the results based on the GM model are in a reasonable agreement with the MD ones. Comparing the ACs presented in Table III with the ones for the fully equilibrium system in Table II, it can be deduced that

imposing a velocity at walls resulted in decreasing the value of all the ACs. In addition, increasing the velocity ratio from  $S_v = 0.2$  to 0.4, the value of  $\alpha_{tot}$  decreased by half. This inverse correlation was also observed by Uene *et al.*<sup>51</sup>

The scattering plots obtained from the GSI models together with the reference MD solutions for the combined Fourier–Couette flow problem ( $S_v = 0.4$ ) at the top wall of the system are depicted in Fig. 6. Again, it is seen that the results from the GM model are in a good agreement with the MD results. On the other hand, the CLL model except for the rotational energy mode does not show a good performance in predicting the other energy modes, as well as the translational velocity components. Similar to the previous case study, for the tangential velocity components, the sharper tips of the velocity clouds along the diagonal lines observed in MD data are captured just by the GM model and cannot be seen in the CLL model results.

The computed KLDs for this case are presented in Fig. 4(c). Significant difference between the performance of the employed GSI models has been observed also here. For example, KLDs for  $E_{tr}$  and  $E_{tot}$  obtained from CLL are 3 orders of magnitudes larger than the corresponding values obtained from the GM model. With regard to  $V_x, V_y, V_z,$  and  $E_{rot}$  the computed values based on the CLL model are 2 orders of magnitudes larger than GM results.

The ACs associated with different velocity components and energy modes for the combined Fourier–Couette flow system are listed in Table IV. It is shown that, similar to the previous case studies, both GSI models have an acceptable accuracy in predicting  $\alpha_x, \alpha_y, \alpha_z,$  and  $\alpha_{rot}$ . However, while the GM model results for  $\alpha_{tr}$  and  $\alpha_{tot}$  are just slightly higher than the MD results, there is a significant discrepancy between the results obtained from the CLL model and MD simulations. Comparing the results shown in Tables IV with those in III and II, the first observation is that in general the ACs in the combined Fourier–Couette flow case studies are lower. In fact, having the top wall at higher temperature together with imposing a wall velocity transfers considerable amount of kinetic energy to the gas domain, which leads to less accommodation of the gas molecules at the walls surface. The second observation is related to the performance of the GM model across these three case studies. Comparing the values of  $\alpha_{tr}$  and  $\alpha_{tot}$  obtained from the MD simulation and the GM model, it is seen that as the system goes toward higher non-equilibrium state, the deviation between the GM model and the original MD results increases.

## 2. $N_2$ –Ni system

The resulting scattering plots of the non-isothermal Fourier thermal problem for the  $N_2$ –Ni system at the top wall are depicted in Fig. 7. It is seen that the correlation graphs and the PDFs of the reflected translational velocity components, as well as the energy modes obtained from both GSI models, match with the atomistic simulation results. The computed KLDs based on the employed scattering models are presented in Fig. 8(a). It is seen that unlike  $H_2$ –Ni system, KLDs obtained from both GSI models are in the same order of magnitude. However, the results of the GM model still show less deviation in comparison with the CLL model (e.g., for  $E_{tot}$ :  $KLD_{CLL} = 2.2 KLD_{GM}$ ). Different ACs obtained for this case study are listed in Table V. It is observed that the ACs based on the GM and CLL scattering models are in good agreement with the reference MD results. However, the value of  $\alpha_{tot}$  predicted by

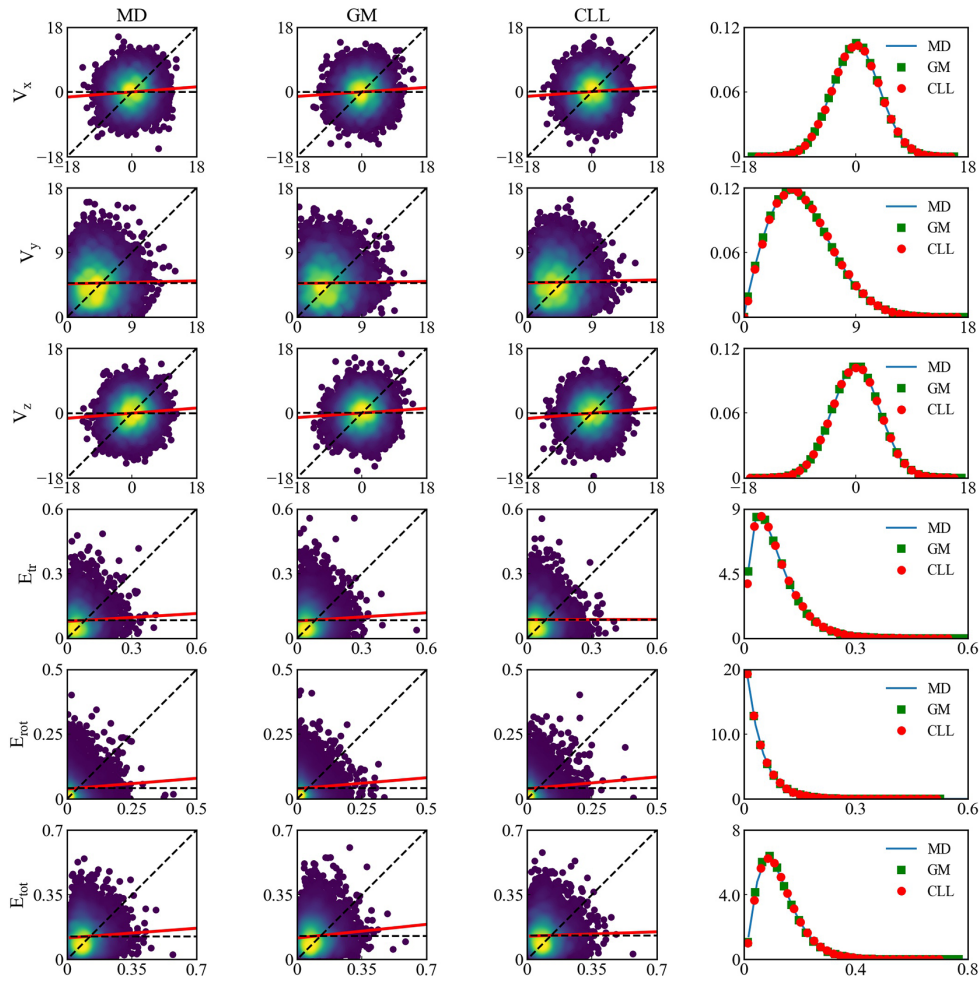


**FIG. 7.** Correlations between incoming (horizontal-axis) and outgoing (vertical-axis) translational velocity components in (Å/ps) and energy modes in (eV) of the non-isothermal Fourier thermal problem for  $N_2$ -Ni system at the top wall. The dashed horizontal and diagonal lines demonstrate fully diffusive and specular reflection, respectively. Solid red lines demonstrate the least-square linear fit of the kinetic data. In the last column, the corresponding probability density functions of the translational velocity components and energy modes for the reflecting particles are presented.

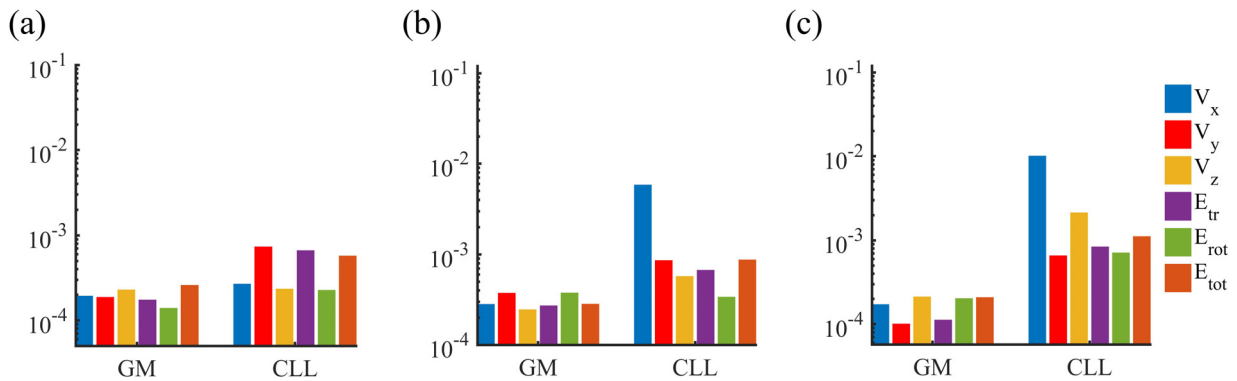


**FIG. 8.** The Kullback-Leibler divergence of the translational velocity components and different energy modes of  $N_2$ -Ni system determined by GM and CLL scattering models; (a) non-isothermal Fourier thermal problem at the top wall; (b) Couette flow problem ( $S_v = 0.4$ ) at the bottom wall; (c) combined Fourier-Couette flow problem ( $S_v = 0.4$ ) at the bottom wall.

**TABLE V.** Tangential momentum ( $\alpha_x, \alpha_z$ ), normal momentum ( $\alpha_y$ ), translational ( $\alpha_{tr}$ ), rotational ( $\alpha_{rot}$ ), and total ( $\alpha_{tot}$ ) energy accommodation coefficients of the Fourier thermal problem for  $N_2$ -Ni system ( $T_b = 300$  K), computed using different scattering kernels: GM and CLL models, and MD simulations. B: bottom wall; T: top wall.

$T_t$	Model	Wall	$\alpha_x$	$\alpha_y$	$\alpha_z$	$\alpha_{tr}$	$\alpha_{rot}$	$\alpha_{tot}$
300	MD	B	0.873	0.965	0.873	0.912	0.863	0.878
	GM	B	0.869	0.968	0.868	0.920	0.881	0.891
	CLL	B	0.871	0.976	0.871	0.976	0.867	0.941
500	MD	B	0.856	0.960	0.857	0.906	0.804	0.855
		T	0.907	0.959	0.916	0.931	0.892	0.903
	GM	B	0.856	0.959	0.855	0.910	0.821	0.886
		T	0.907	0.957	0.912	0.930	0.907	0.912
	CLL	B	0.856	0.966	0.856	0.975	0.802	0.917
		T	0.911	0.968	0.921	0.978	0.888	0.948

**TABLE VI.** Tangential momentum ( $\alpha_x, \alpha_z$ ), normal momentum ( $\alpha_y$ ), translational ( $\alpha_{tr}$ ), rotational ( $\alpha_{rot}$ ), and total ( $\alpha_{tot}$ ) energy accommodation coefficients of the Couette flow problem for  $N_2$ -Ni system at different speed ratios ( $S_v$ ), computed using different scattering kernels: GM and CLL models, and MD simulations.

$S_v$	Model	$\alpha_x$	$\alpha_y$	$\alpha_z$	$\alpha_{tr}$	$\alpha_{rot}$	$\alpha_{tot}$
0.2	MD	0.873	0.968	0.873	0.911	0.857	0.873
	GM	0.874	0.967	0.881	0.910	0.873	0.881
	CLL	0.876	0.975	0.873	0.978	0.864	0.940
0.4	MD	0.865	0.968	0.872	0.917	0.862	0.879
	GM	0.860	0.967	0.867	0.907	0.873	0.874
	CLL	0.864	0.973	0.873	0.974	0.859	0.937

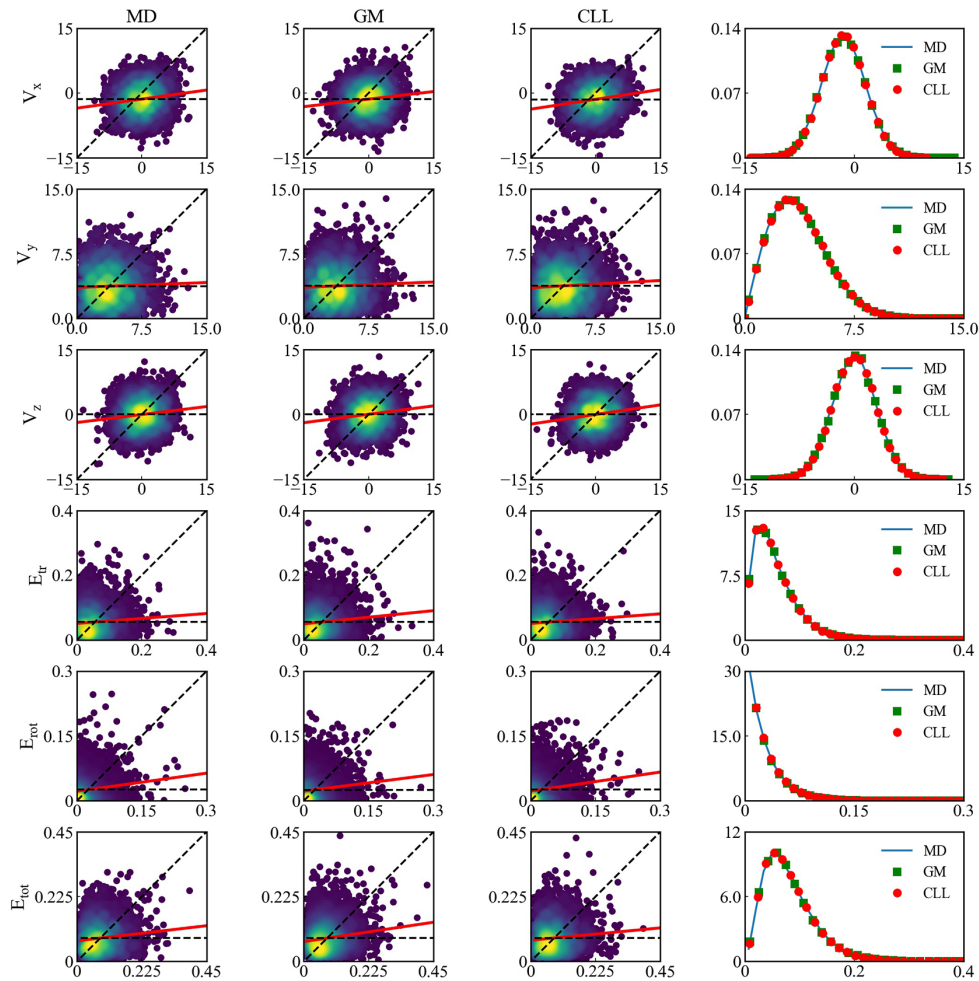


**FIG. 9.** Correlations between incoming (horizontal-axis) and outgoing (vertical-axis) translational velocity components in ( $\text{\AA}/\text{ps}$ ) and energy modes in (eV) of the Couette flow problem ( $S_v = 0.4$ ) for  $N_2$ -Ni system at the bottom wall. The dashed horizontal and diagonal lines demonstrate fully diffusive and specular reflection, respectively. Solid red lines demonstrate the least-square linear fit of the kinetic data. In the last column, the corresponding probability density functions of the translational velocity components and energy modes for the reflecting particles are presented.

the GM model is closer to the MD results in comparison with the CLL model. Furthermore, changing the top wall temperature from  $T_t = 300$  to  $500$  K, so going from the isothermal to the non-isothermal system, did not have any noticeable impact on the values of the ACs. This means that different from  $H_2$ -Ni system, here ACs are not dependent on the temperature in the system.

Figure 9 represents the scattering plots for the Couette flow problem ( $S_v = 0.4$ ) at the bottom wall. It is shown that all velocity components, as well as the energy modes predicted by the scattering models, agree well with the MD results. However, in the  $x$  direction, the original MD and GM results are more skewed, while the correlation graph obtained from the CLL model seems very symmetric around the horizontal dashed line. The computed KLDs for this case study [see Fig. 8(b)] also confirm the observed discrepancies in the scattering plots. It is shown that the measured KLD for  $V_x$  based on the CLL model is the highest one. The impact of such deviation can be seen also in relatively larger values of  $E_{tr}$  and  $E_{tot}$  obtained from the CLL scattering model.

Different ACs for the Couette flow system are listed in Table VI. Similar to the previous case study, quite acceptable performance in terms of predicting ACs was observed from the GSI models. Furthermore, based the reported values in Tables V and VI, it can be deduced that neither imposing velocity at walls nor increasing the velocity ratio from  $S_v = 0.2$  to  $0.4$  have any noticeable impact on the values of the ACs.

The correlations and PDF graphs for the Fourier-Couette flow problem at the bottom wall ( $S_v = 0.4$ ) are depicted in Fig. 10. From this figure, the most notable difference between the performance of the employed GSI models is seen just in the shape of the clouds in the tangential directions. It is shown that the tips of the  $V_x$  and  $V_z$  components obtained from MD simulations and the GM model at high velocities are sharper than the CLL results. In addition, the overall shape of the clouds for  $V_x$  from MD simulations and GM are not symmetric, while the  $V_x$  component obtained from the CLL model is symmetric around the horizontal dashed line. The KLDs for this case study are presented in Fig. 8(c). Similar to the previous case studies, superior performance of the

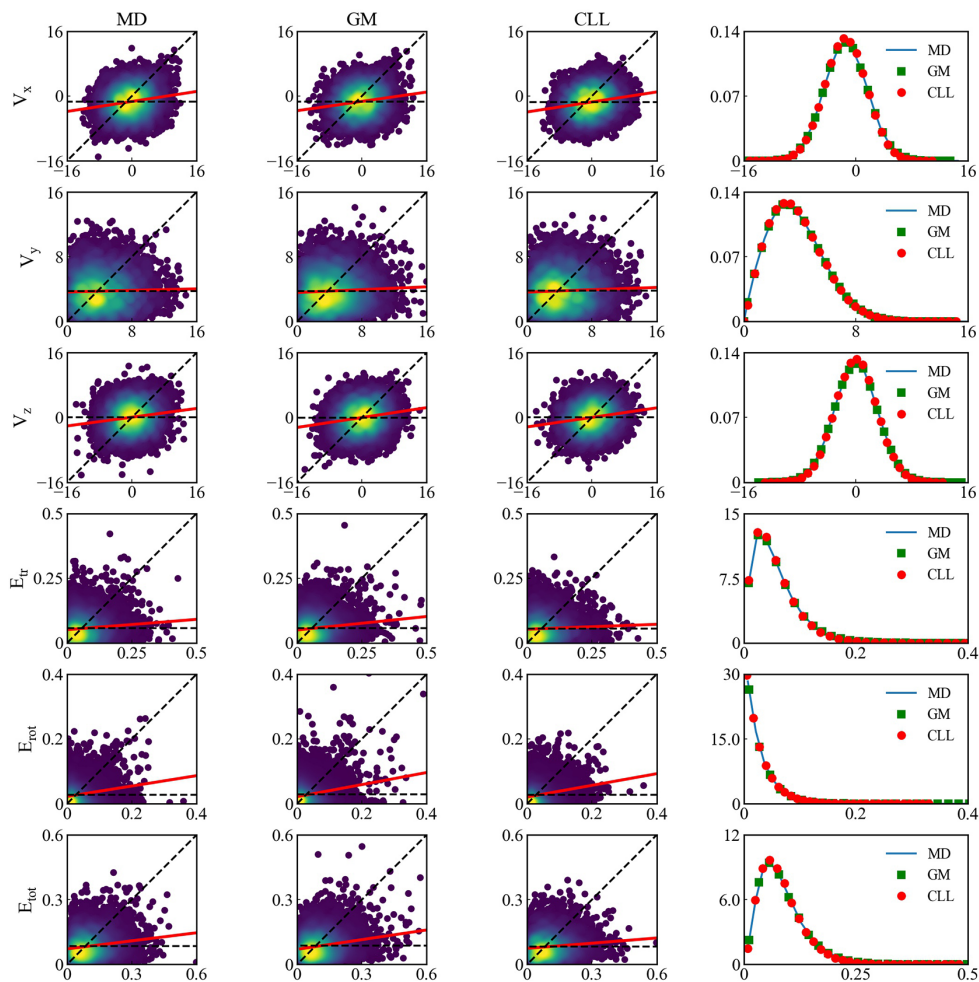


**FIG. 10.** Correlations between incoming (horizontal-axis) and outgoing (vertical-axis) translational velocity components in ( $\text{\AA}/\text{ps}$ ) and energy modes in (eV) of combined Fourier-Couette flow problem for  $N_2$ -Ni system at the bottom wall ( $S_w = 0.4$ ). The dashed horizontal and diagonal lines demonstrate fully diffusive and specular reflection, respectively. Solid red lines demonstrate the least-square linear fit of the kinetic data. In the last column, the corresponding probability density functions of the translational velocity components and energy modes for the reflecting particles are presented.

**TABLE VII.** Tangential momentum ( $\alpha_x, \alpha_z$ ), normal momentum ( $\alpha_y$ ), translational ( $\alpha_{tr}$ ), rotational ( $\alpha_{rot}$ ), and total ( $\alpha_{tot}$ ) energy accommodation coefficients of the combined Fourier–Couette flow problem for  $N_2$ –Ni system at different speed ratios ( $S_v$ ), computed using different scattering kernels: GM and CLL models, and MD simulations. B: bottom wall; T: top wall.

$S_v$	Model	Wall	$\alpha_x$	$\alpha_y$	$\alpha_z$	$\alpha_{tr}$	$\alpha_{rot}$	$\alpha_{tot}$
0.2	MD	B	0.856	0.959	0.855	0.907	0.812	0.856
		T	0.902	0.960	0.908	0.931	0.894	0.903
	GM	B	0.856	0.960	0.856	0.907	0.829	0.863
		T	0.906	0.958	0.916	0.934	0.904	0.904
	CLL	B	0.856	0.961	0.858	0.971	0.814	0.921
		T	0.906	0.954	0.909	0.972	0.899	0.946
0.4	MD	B	0.850	0.962	0.856	0.904	0.812	0.855
		T	0.910	0.967	0.908	0.934	0.897	0.906
	GM	B	0.849	0.962	0.852	0.908	0.831	0.867
		T	0.909	0.965	0.906	0.932	0.905	0.906
	CLL	B	0.853	0.966	0.856	0.975	0.809	0.923
		T	0.917	0.973	0.909	0.980	0.894	0.947

GM model can be also noticed here. Comparing the KLDs from CLL in this case study with the ones for the Couette flow problem [see Fig. 8(b)], it can be inferred that imposing a wall velocity together with having walls with different temperatures induced larger deviation of the CLL predictions from the reference MD results. The calculated ACs for this case are listed in Table VII. Again, it is seen that both GSI models can predict ACs with good accuracy. However, the value of  $\alpha_{tot}$  obtained from the GM model has a slightly better agreement with the MD results as compared with the value obtained from the CLL model. Comparing the results at different velocity ratios, it can be argued that similar to the Couette flow problem, here also increasing the velocity ratio merely affects the values of the ACs, which was different in the case of  $H_2$ –Ni system. Looking to the original MD data, the possible reasons for

different thermal behaviors of the reflected  $H_2$  and  $N_2$  molecules are discussed in Sec. III C.

### C. Impact of the adsorption layer on behavior of reflected gas molecules

In this part, the MD simulation results for  $H_2$ –Ni and  $N_2$ –Ni systems are studied more elaborately, in order to gain further insight on the behavior of  $H_2$  and  $N_2$  under different thermal and flow conditions. Here, the variation of the local number density of the gases across the channel height ( $y$  direction) is examined for each benchmark problem. The results for  $H_2$ –Ni are shown in Fig. 11. It is seen that for the systems, in which both walls have the same temperature [see Fig. 11(a)], in general, the density near the walls is higher than the bulk density. The density peak at the gas–solid interface indicates the physical adsorption of the gas molecules at the solid surface. This has been also observed previously.<sup>52,53</sup> It is seen in this figure that by imposing velocity at the walls the density peaks near the walls are diminishing, and at  $S_v = 0.4$ , the density peaks are lowest. In fact, increasing  $S_v$  causes a lower residence time of gas molecules at the surface. For instance, for the isothermal Fourier thermal problem the residence time ( $t_{RES}$ ) is 1270 ps, while for the Couette flow problem with  $S_v = 0.4$ , the obtained value is  $t_{RES} = 957$  ps. The gas adsorption layer inducing a longer gas–solid interaction time leads to an increased heat transfer at the boundary layer. Higher ACs obtained for the Fourier thermal problem in comparison with the Couette flow problem (see Tables II and III) also confirm this effect. The number density profiles for  $H_2$ –Ni benchmark systems with the walls at different temperatures are presented in Fig. 11(b). It is shown that at the bottom wall ( $T_b = 300$  K), the density peak is higher than the density peak at the top wall ( $T_t = 500$  K). However, similar to the isothermal walls systems, the reducing effect of the imposed wall velocity on the magnitude of the density peaks adjacent to the walls is also observed here. For the combined Fourier–Couette flow problem ( $S_v = 0.4$ ) at the top wall, the value of the number density is even lower than the bulk value. Such behavior has not been observed previously. However, it is noteworthy to mention that, due to high surface

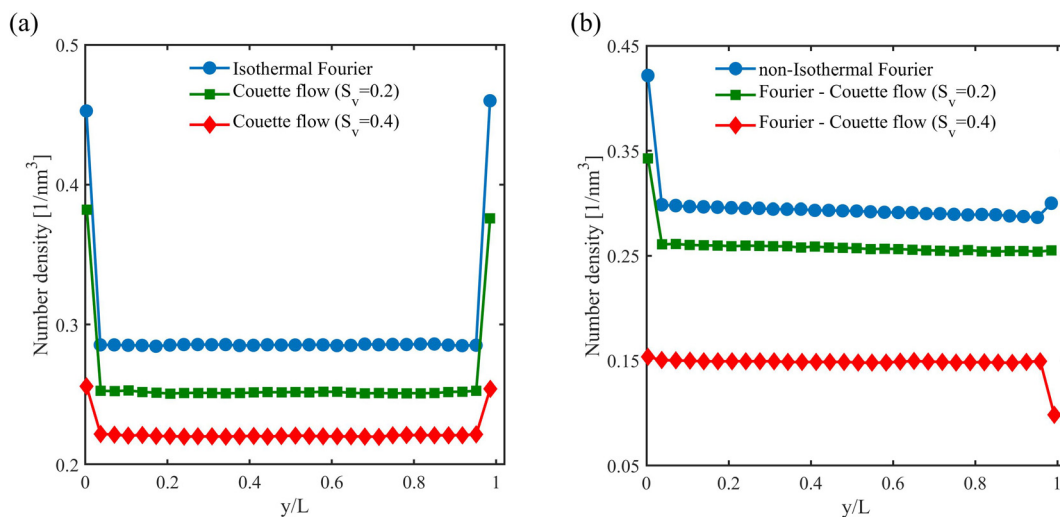


**FIG. 11.** Number density profiles for  $H_2$ –Ni system with (a) isothermal walls ( $T_b = T_t = 300$  K); (b) non-isothermal walls ( $T_b = 300$ ,  $T_t = 500$  K).



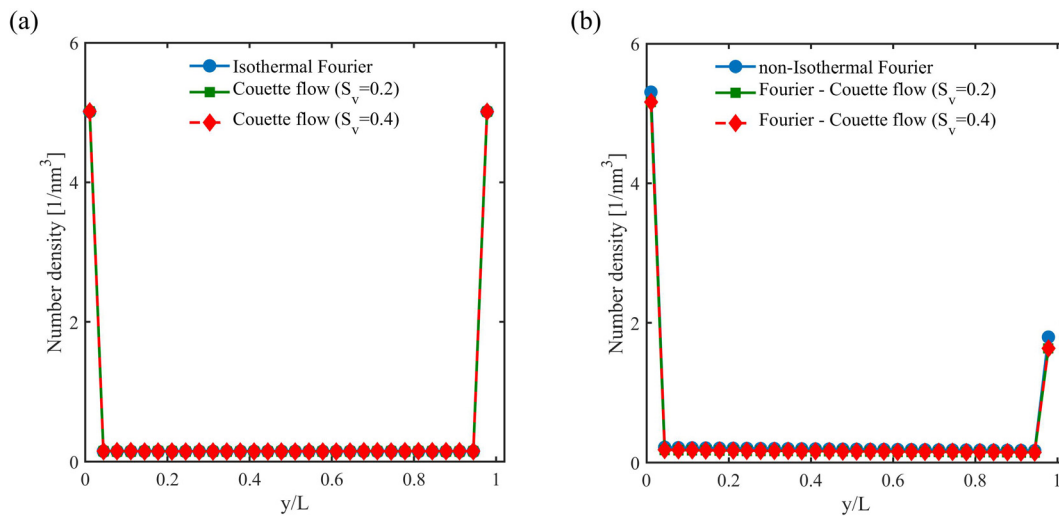


FIG. 12. Number density profiles for  $N_2$ -Ni system with (a) isothermal walls ( $T_b = T_t = 300$  K); (b) non-isothermal walls ( $T_b = 300$ ,  $T_t = 500$  K).

temperature in combination with a high wall velocity ( $u_w = 629$  m/s), an enormous amount of the kinetic energy is added to the gas molecules. Such an extreme situation cannot be studied experimentally, and the main objective of choosing it in this work was the trend study of the scattering models. The obtained ACs for this case are the lowest among the all studied cases for  $H_2$ -Ni system.

Figure 12 represents the local number density variations of different case studies for  $N_2$ -Ni system. The molecular mass of  $N_2$  is considerably higher than  $H_2$  ( $m_{N_2} = 14m_{H_2}$ ). This fact together with a stronger gas-wall interaction potential between  $N_2$  and Ni leads to more predominant adsorption for  $N_2$  molecules. This can be also deduced from the considerable deviation of the number density in the vicinity of the walls from the bulk number density, as shown in Fig. 12. Furthermore, the formed layer is strongly attached to Ni surface. Unlike  $H_2$ -Ni system, imposing a velocity at the walls does not have any noticeable impact on the density profiles. However, in the case of the system with non-isothermal walls [see Fig. 12(b)] the number density at the top hot wall is lower than the bottom cold wall, and this trend is in accordance with the one already observed for  $H_2$ -Ni system.

As already mentioned, higher adsorption of gas molecules at the surface causes an enhancement in thermal energy exchange at the gas-solid interface. However, it was observed by Sun *et al.*<sup>53</sup> that there is a limit for such enhancement. Basically, when the solid surface is fully covered by gas molecules and there is no more space for further adsorption, the energy transport properties do not increase anymore. In fact, under such circumstances, gas phase molecules actually collide mainly with the other gas molecules present in the gas layer at the solid surface. Consequently, there is no further energy exchange caused by gas-wall interactions. Our results show that for  $N_2$ -Ni system, the solid surface is fully saturated with gas molecules, and the interfacial heat transfer is highly dominated by the presence of the gas adsorbed layer. Therefore, changing the characteristics of the system such as imposing a velocity at the wall or increasing the wall temperature does not have any significant impact on the thermal properties of  $N_2$  molecules after colliding with the Ni surface. This is also reflected in the values of various ACs in different case studies for  $N_2$ -Ni system reported in Sec. III B 2 that are very close

to each other. On the other hand, in the case of  $H_2$ -Ni system, the adhesion force between  $H_2$  molecules and Ni surface is very weak, which is mainly due to the relatively low weight of  $H_2$  molecules. Hence, the thermal characteristics of the  $H_2$ -Ni interface are very likely to change by imposing some perturbations in the system. This can be also realized by different shapes of the correlation graphs, as well as different values of computed ACs for the various studied benchmark systems in Sec. III B 1.

#### IV. CONCLUSIONS

In this work, an unsupervised machine learning technique, known as the GM model, is applied to construct a scattering model for diatomic gas molecules ( $H_2$ ,  $N_2$ ) interacting with the solid Ni surface. The main reason behind using this specific technique is that GM is considered as one of the most efficient probabilistic machine learning techniques that can be used to cluster a general dataset, in which the subsets follow Gaussian distributions. The GM scattering model is constructed from the superposition of  $K$  multidimensional Gaussian functions, each determined by a mean vector and covariance matrix. Therefore, the GM scattering model is categorized as a parametric model. However, since the number of employed parameters is not limited as the classical parametric scattering kernels, the GM model is much more flexible. Here, the entire incoming and outgoing translational and rotational velocity components obtained from the MD simulations are used for training of the model. This guarantees that the model is able to describe all possible phenomena caused by inelastic gas-surface collisions when the system is in a highly non-equilibrium condition.

Using the original MD simulation results for  $H_2$ -Ni and  $N_2$ -Ni as reference solutions, the performance of the GM scattering model is compared with the CLL scattering model in different thermal problems that are commonly faced in rarefied gas flow systems. It is observed that for  $H_2$ -Ni changing the wall temperature or imposing an external velocity at the walls considerably affects the behavior of postcollisional gas molecules. While the GM scattering model can predict such behavior with good accuracy, the results of the CLL model in non-equilibrium conditions highly deviate from the MD results. Nevertheless, by going toward extremely non-equilibrium situations,

the performance of the GM model slightly degrades, but it still outperforms the CLL model.

On the other hand, for  $N_2$ -Ni case, changing the system characteristics does not have a noticeable impact on the kinetic features of  $N_2$  molecules after reflecting from the surface. Here, the shape of the correlation graphs, the PDF of the outgoing translational velocity components and energy modes, and the computed ACs in different benchmark systems remain more or less the same. In this case, in general, the predictions from both the employed stochastic scattering models are in a good agreement with the MD results. However, also here the GM results are slightly in better agreement with the MD data.

To shed some lights on the possible reasons behind very different behaviors of  $H_2$  and  $N_2$  gases in the studied systems, the variation of the local number density of the gas molecules in each system obtained from the conducted MD simulations has been investigated. It is observed that in the case of  $N_2$ -Ni, the solid surface is saturated with gas molecules and applying different perturbations at the walls, such as increasing the temperature or imposing an external velocity, does not have a considerable impact on the amount of adsorbed gas molecules. Consequently, the incoming gas molecules from the bulk of the gas toward the surface mainly encounter other gas molecules that are stuck at the surface, and they do not really exchange energy with Ni molecules. However, for the  $H_2$ -Ni the adsorption layer is less dominant. As a result, changing wall features (temperature or velocity) has relatively more impacts on the behavior of reflected gas molecules in the case of  $H_2$  than for  $N_2$ .

The observed high precision of the GM predictions indicates that it can be considered a promising candidate to compute important discontinuity phenomena such as temperature jump and velocity slip in rarefied gas flow systems. In addition, the accuracy of the GM model results indicates the high potential of this approach to construct a generalized scattering kernel for diatomic gas–solid surface interactions. Nevertheless, a more extended dataset, including a wider range of wall temperatures and gas densities, is required to construct such a model. Further studies will be devoted to these problems.

### ACKNOWLEDGMENTS

This work is part of the research program RareTrans with Project No. HTSM-15376, which is (partly) financed by the Netherlands Organization for Scientific Research (NWO).

### AUTHOR DECLARATIONS

#### Conflict of Interest

The authors have no conflicts to disclose.

#### Author Contributions

**Shahin Mohammad Nejad:** Data curation (lead); Formal analysis (lead); Investigation (lead); Methodology (lead); Software (lead); Validation (lead); Visualization (lead); Writing – original draft (lead); Writing – review & editing (equal). **Silvia V. Gaastra-Nedea:** Project administration (equal); Resources (equal); Supervision (equal); Writing – review & editing (equal). **Arjan J. H. Frijns:** Funding acquisition (equal); Project administration (equal); Resources (lead); Supervision (lead); Writing – review & editing (lead). **David Smeulders:** Funding acquisition (equal); Project administration (equal); Resources (equal); Supervision (supporting); Writing – review & editing (equal).

#### DATA AVAILABILITY

The data that support the findings of this study are available from the corresponding author upon reasonable request.

### APPENDIX A: SENSITIVITY ANALYSIS IN ORDER TO DECIDE THE NUMBER OF GAUSSIAN FUNCTIONS (K) USED IN THE GM MODEL

In the case of the GM model, a sensitivity analysis is needed to select the optimal number of the Gaussian functions. Here, for both gas–solid pairs, the isothermal Fourier thermal problem without any heat flux ( $T_b = T_t = 300$  K) is chosen as the benchmark system. Afterward, the number of Gaussians  $K$  is varied in the range of

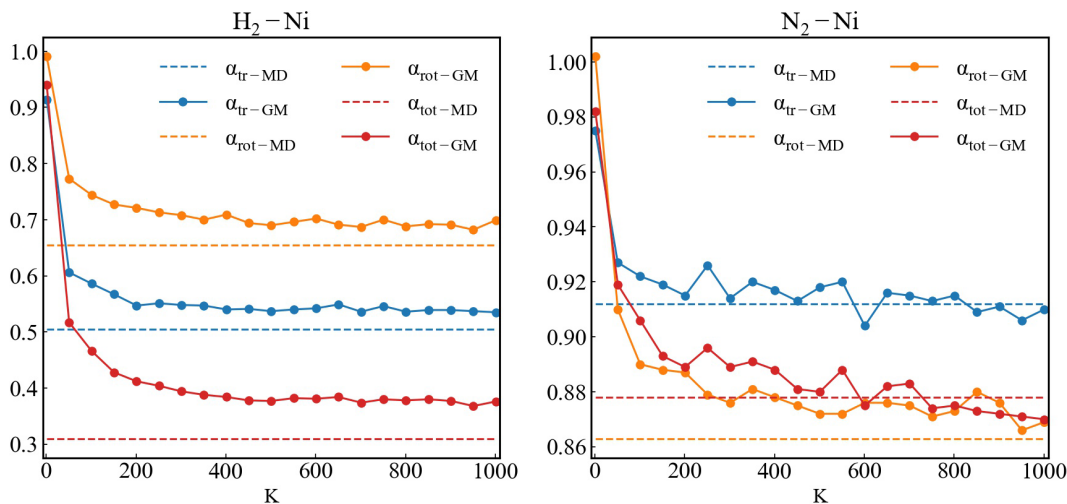


**FIG. 13.** Accommodation coefficients related to the translational energy ( $\alpha_{tr}$ ), rotational energy ( $\alpha_{rot}$ ), and total energy ( $\alpha_{tot}$ ) computed using atomistic simulations and the GM scattering model using different number of Gaussian functions  $K$ .

$K = 1-1000$ , and the ACs for different gas molecule's energy modes consist of the translational energy AC ( $\alpha_{tr}$ ), the rotational energy AC ( $\alpha_{rot}$ ), and the total energy AC ( $\alpha_{tot}$ ) driven from the GM model are compared with the corresponding values obtained from the original MD data. From Fig. 13, it can be understood that for  $H_2-Ni$  system, there is no considerable change in the values of the ACs for  $K \geq 500$ . Therefore,  $K = 500$  is used as the number of Gaussian functions in the GM model in the case of  $H_2-Ni$  system. The results for  $N_2-Ni$  system are illustrated in Fig. 13. In this case study for  $K \geq 100$ , already the difference between all the computed ACs based on the GM model and the MD results is less than 5%. However, considering more importance for the total energy AC, the

smallest  $K$  at which the difference between the GM model and MD results is the lowest ( $K = 450$ ) is used as the number of Gaussians for training the GM model based on the results from  $N_2-Ni$  system.

**APPENDIX B: CORRELATION GRAPHS AND PDFS OF THE H2-NI CASE STUDIES**

In this appendix, the correlations between incoming and outgoing velocities, energy modes, and the corresponding probability density functions for the  $H_2-Ni$  system are shown for the non-isothermal Fourier problem (Fig. 14), Couette flow problem ( $S_v = 0.2$ ) (Fig. 15) and combined Fourier-Couette flow problems (Fig. 16-18).

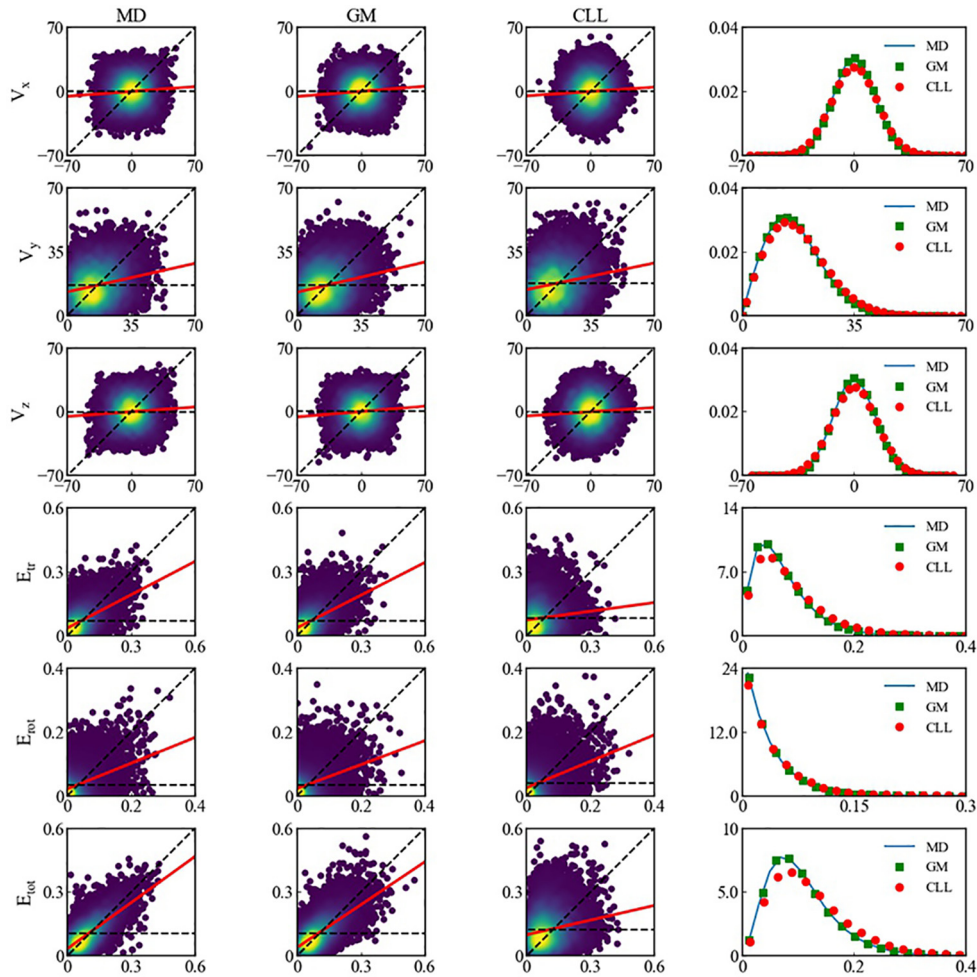


**FIG. 14.** Correlations between incoming (horizontal-axis) and outgoing (vertical-axis) translational velocity components in ( $\text{\AA}/\text{ps}$ ) and energy modes in (eV) of the non-isothermal Fourier thermal problem for  $H_2-Ni$  system at the top wall. The dashed horizontal and diagonal lines demonstrate fully diffusive and specular reflection, respectively. Solid red lines demonstrate the least-square linear fit of the kinetic data. In the last column, the corresponding probability density functions of the translational velocity components and energy modes for the reflecting particles are presented.

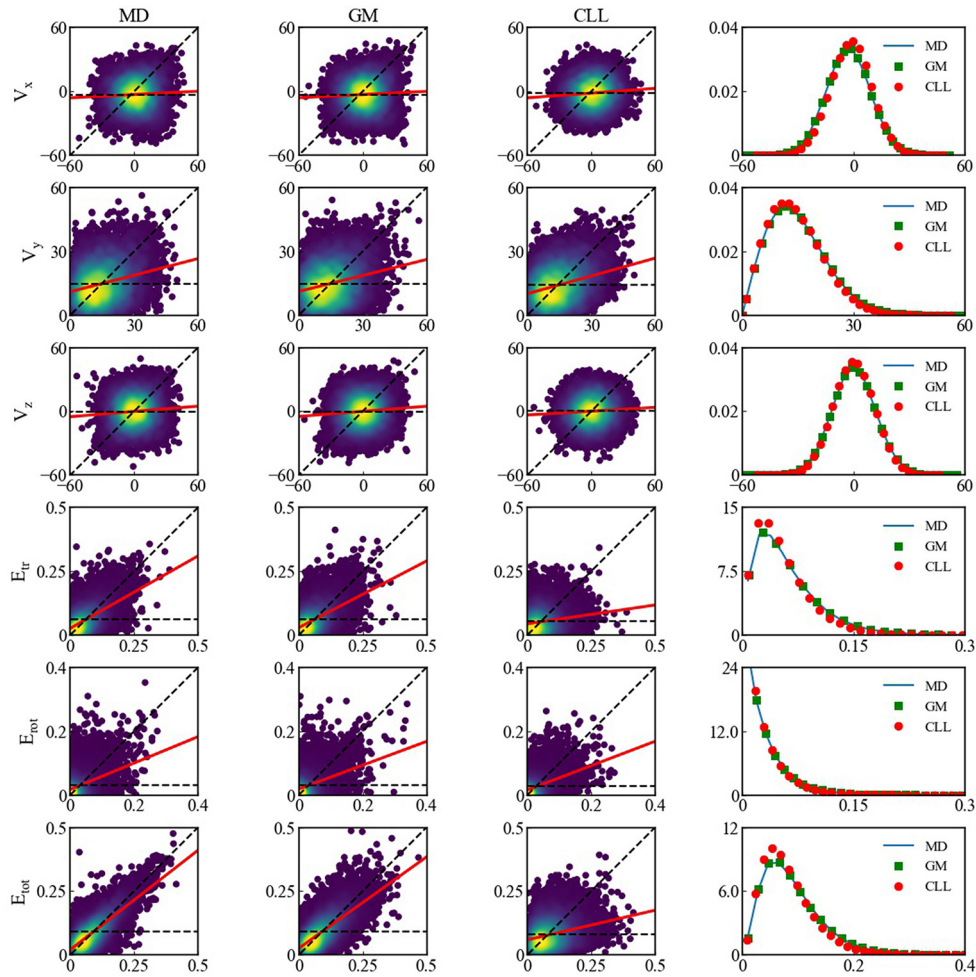


**FIG. 15.** Correlations between incoming (horizontal-axis) and outgoing (vertical-axis) translational velocity components in ( $\text{\AA}/\text{ps}$ ) and energy modes in (eV) of the Couette flow problem ( $S_v = 0.2$ ) for  $\text{H}_2$ -Ni system at the bottom wall. The dashed horizontal and diagonal lines demonstrate fully diffusive and specular reflection, respectively. Solid red lines demonstrate the least-square linear fit of the kinetic data. In the last column, the corresponding probability density functions of the translational velocity components and energy modes for the reflecting particles are presented.

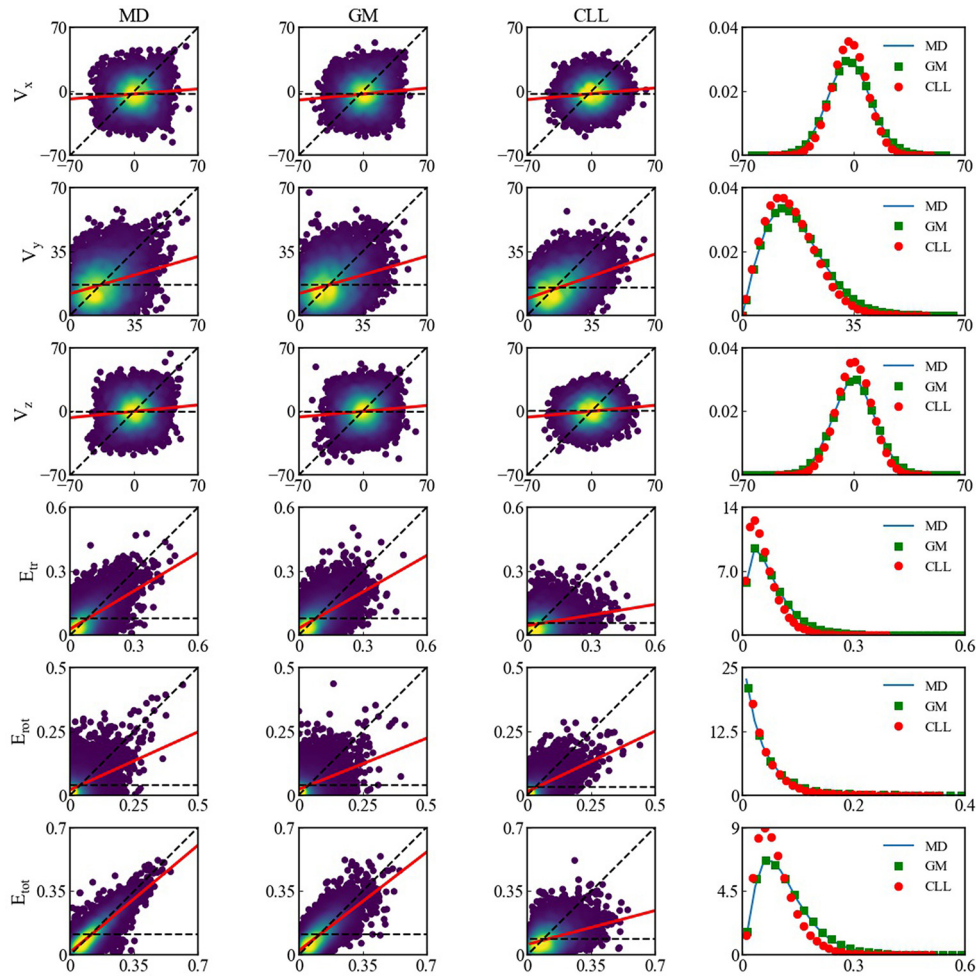


**FIG. 16.** Correlations between incoming (horizontal-axis) and outgoing (vertical-axis) translational velocity components in ( $\text{\AA}/\text{ps}$ ) and energy modes in (eV) of combined Fourier–Couette flow problem for  $\text{H}_2\text{--Ni}$  system at the bottom wall ( $S_w = 0.2$ ). The dashed horizontal and diagonal lines demonstrate fully diffusive and specular reflection, respectively. Solid red lines demonstrate the least-square linear fit of the kinetic data. In the last column, the corresponding probability density functions of the translational velocity components and energy modes for the reflecting particles are presented.

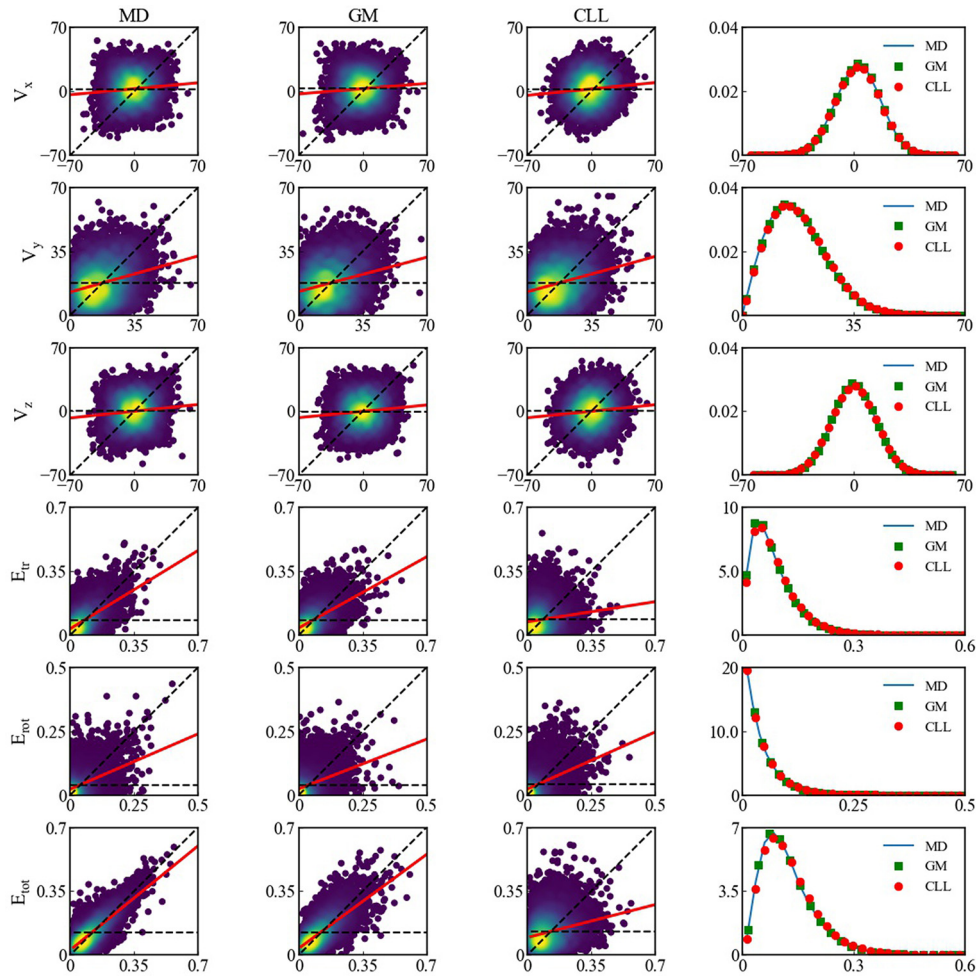


**FIG. 17.** Correlations between incoming (horizontal-axis) and outgoing (vertical-axis) translational velocity components in ( $\text{\AA}/\text{ps}$ ) and energy modes in (eV) of combined Fourier–Couette flow problem for  $\text{H}_2$ –Ni system at the top wall ( $S_v = 0.2$ ). The dashed horizontal and diagonal lines demonstrate fully diffusive and specular reflection, respectively. Solid red lines demonstrate the least-square linear fit of the kinetic data. In the last column, the corresponding probability density functions of the translational velocity components and energy modes for the reflecting particles are presented.

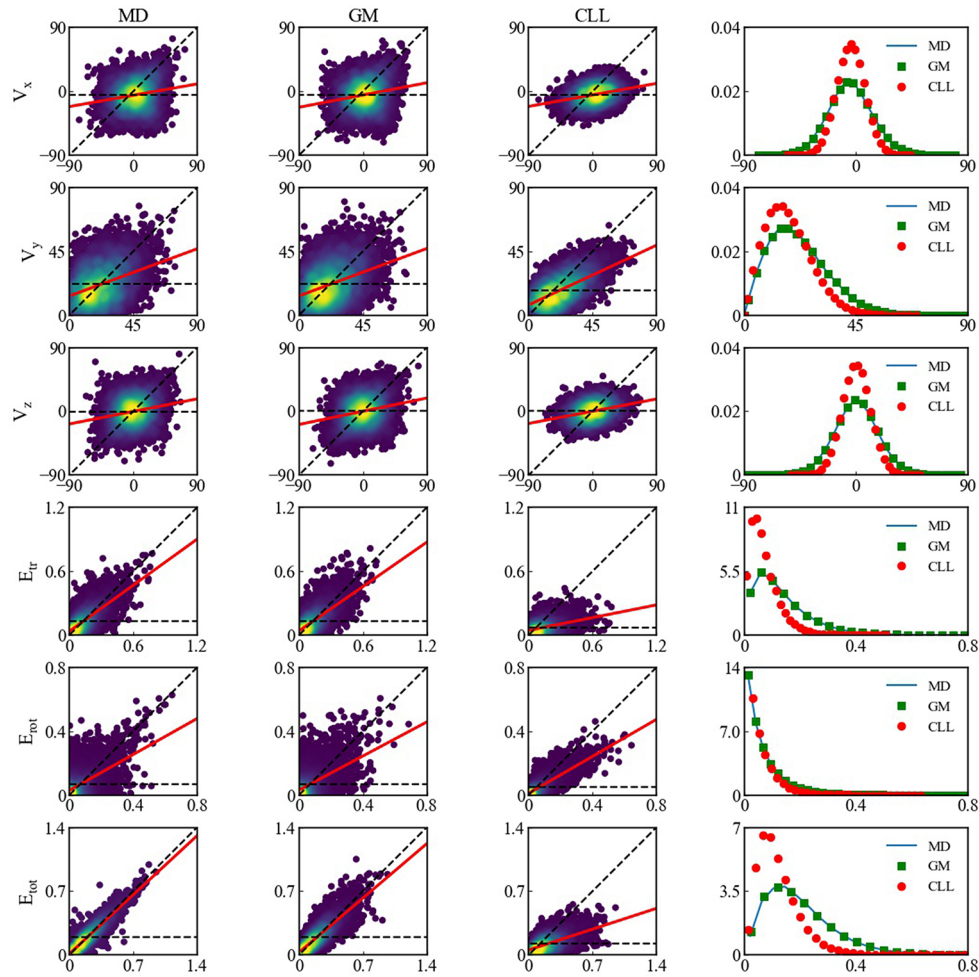


**FIG. 18.** Correlations between incoming (horizontal-axis) and outgoing (vertical-axis) translational velocity components in ( $\text{\AA}/\text{ps}$ ) and energy modes in (eV) of combined Fourier–Couette flow problem for  $\text{H}_2$ –Ni system at the bottom wall ( $S_w = 0.4$ ). The dashed horizontal and diagonal lines demonstrate fully diffusive and specular reflection, respectively. Solid red lines demonstrate the least-square linear fit of the kinetic data. In the last column, the corresponding probability density functions of the translational velocity components and energy modes for the reflecting particles are presented.

**APPENDIX C: CORRELATION GRAPHS AND PDFS OF THE N<sub>2</sub>-NI CASE STUDIES**

In this appendix, the correlations between incoming and outgoing velocities, energy modes, and the corresponding

probability density functions for the N<sub>2</sub>-Ni system are shown for the isothermal Fourier problem (Fig. 19), the non-isothermal Fourier thermal problem (Fig. 20), Couette flow problem ( $S_b = 0.2$ ) (Fig. 21) and combined Fourier-Couette flow problem (Figs. 22–24).

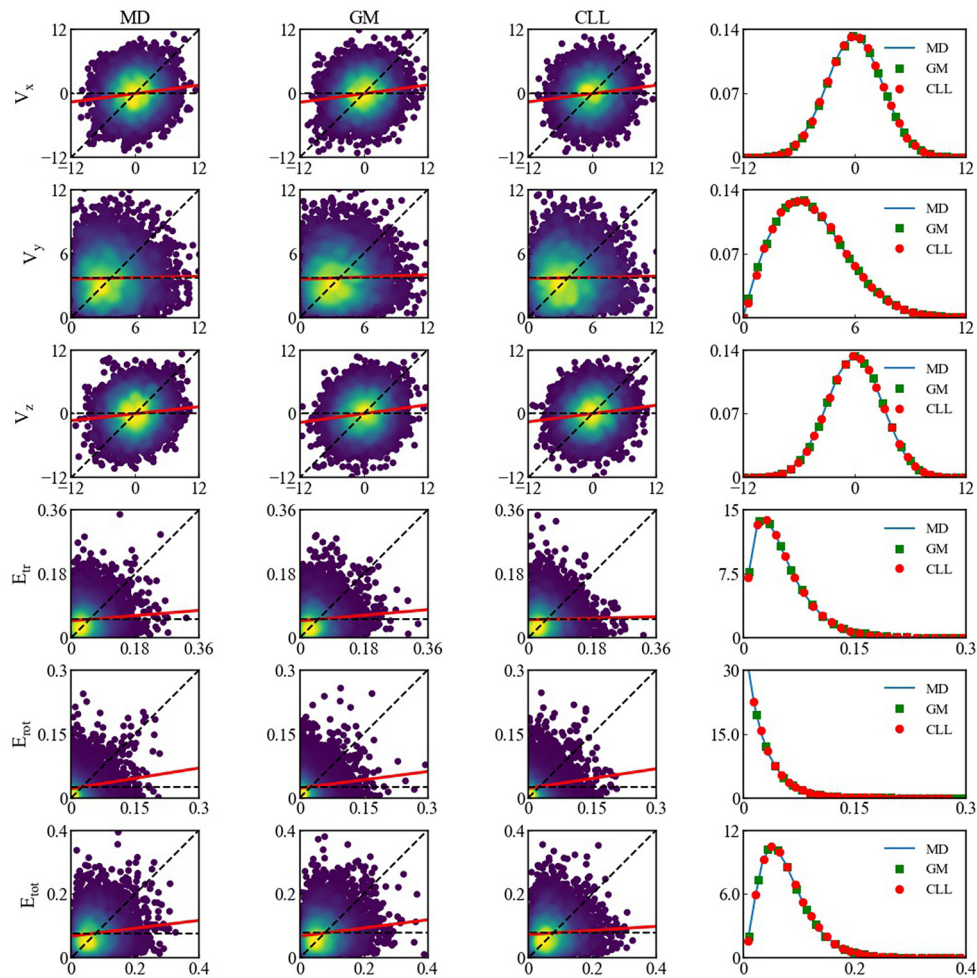


**FIG. 19.** Correlations between incoming (horizontal-axis) and outgoing (vertical-axis) translational velocity components in ( $\text{\AA}/\text{ps}$ ) and energy modes in (eV) of the isothermal Fourier thermal problem for N<sub>2</sub>-Ni system at the bottom wall. The dashed horizontal and diagonal lines demonstrate fully diffusive and specular reflection, respectively. Solid red lines demonstrate the least-square linear fit of the kinetic data. In the last column, the corresponding probability density functions of translational velocity components and energy modes for the reflecting particles are presented.



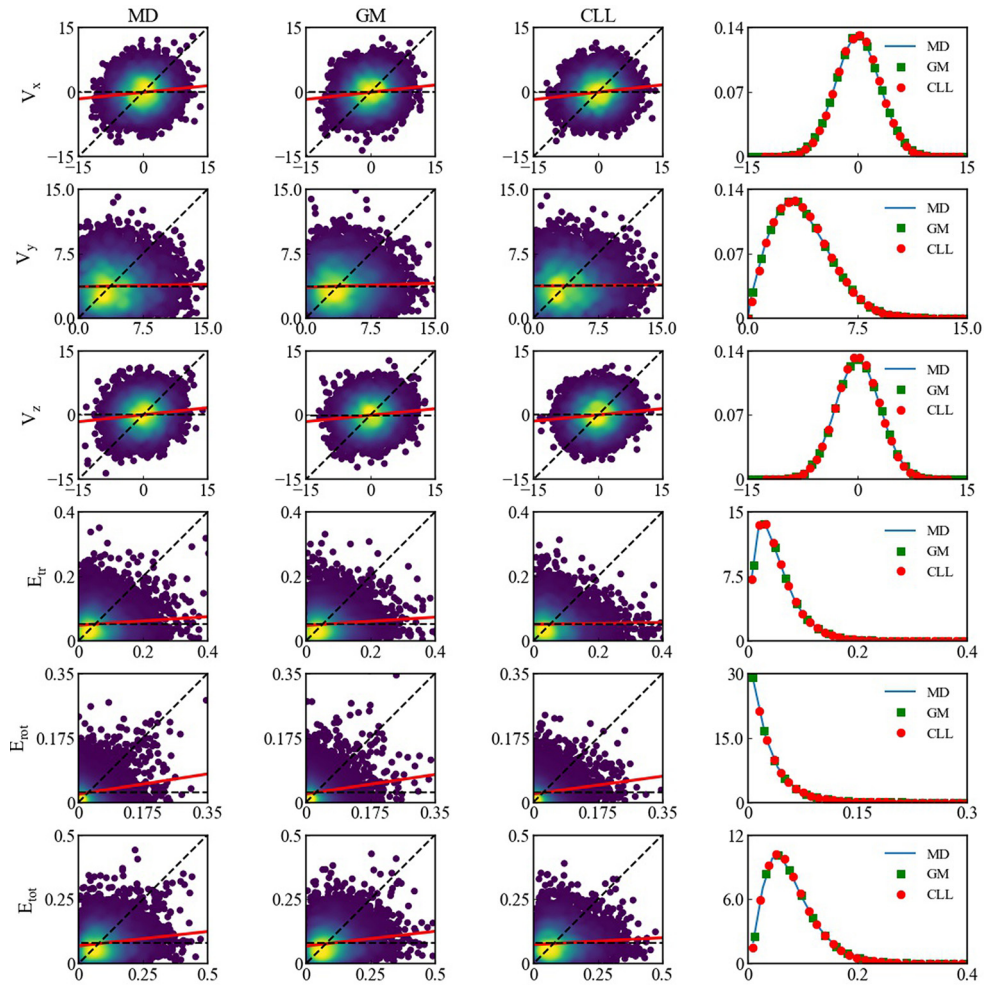


**FIG. 20.** Correlations between incoming (horizontal-axis) and outgoing (vertical-axis) translational velocity components in ( $\text{\AA}/\text{ps}$ ) and energy modes in (eV) of the non-isothermal Fourier thermal problem for  $\text{N}_2$ -Ni system at the bottom wall. The dashed horizontal and diagonal lines demonstrate fully diffusive and specular reflection, respectively. Solid red lines demonstrate the least-square linear fit of the kinetic data. In the last column, the corresponding probability density functions of the translational velocity components and energy modes for the reflecting particles are presented.

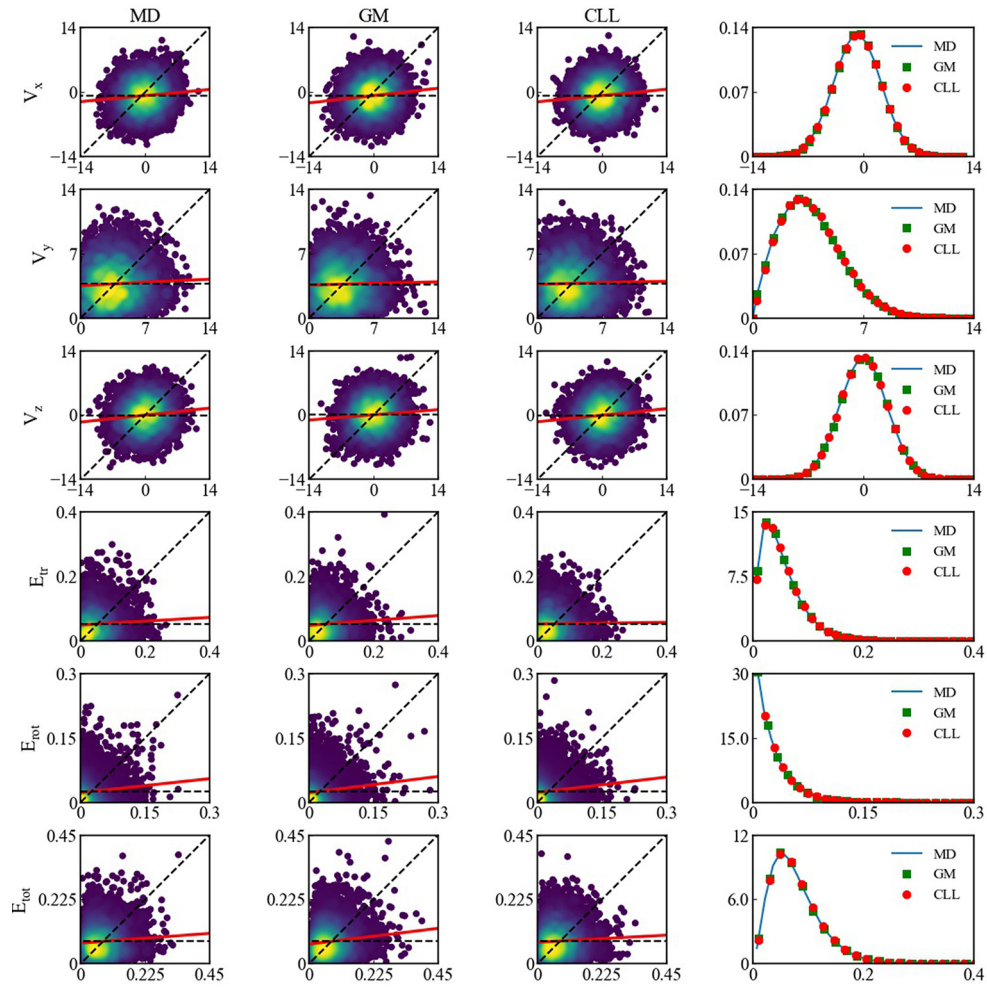


**FIG. 21.** Correlations between incoming (horizontal-axis) and outgoing (vertical-axis) translational velocity components in ( $\text{\AA}/\text{ps}$ ) and energy modes in (eV) of the Couette flow problem ( $S_w = 0.2$ ) for  $\text{N}_2$ -Ni system at the bottom wall. The dashed horizontal and diagonal lines demonstrate fully diffusive and specular reflection, respectively. Solid red lines demonstrate the least-square linear fit of the kinetic data. In the last column, the corresponding probability density functions of the translational velocity components and energy modes for the reflecting particles are presented.

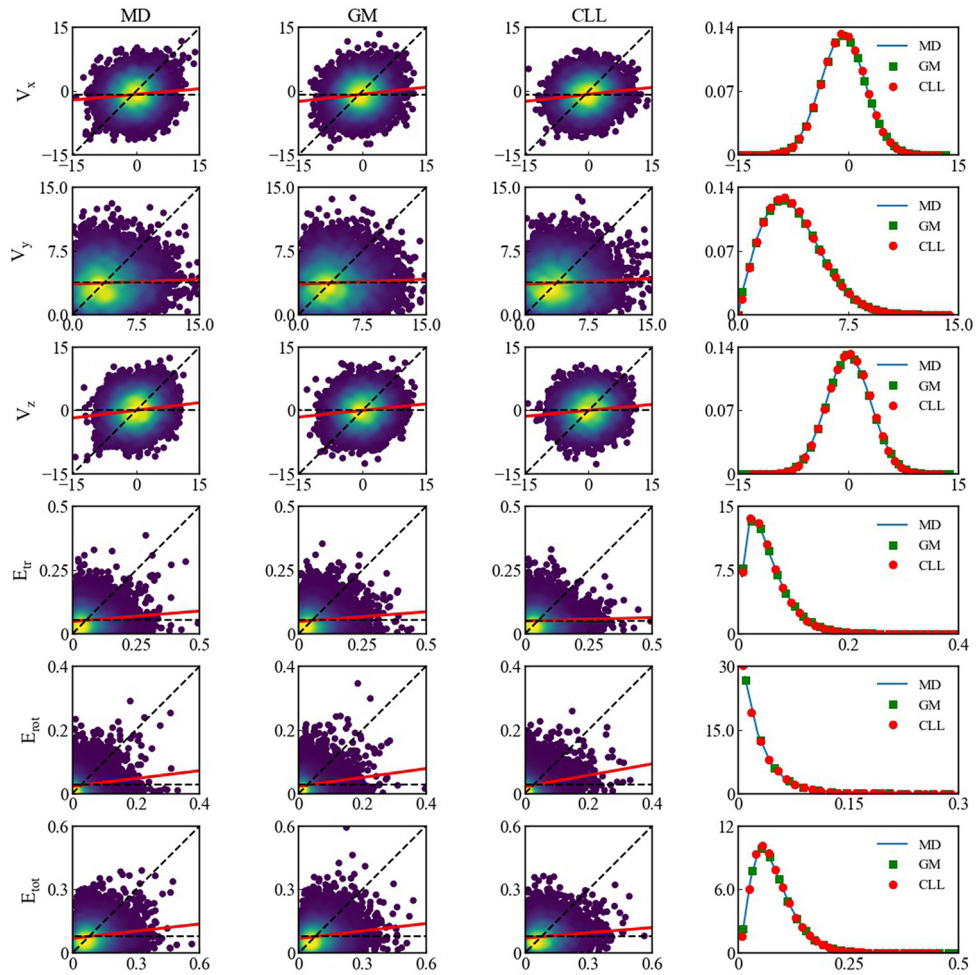


**FIG. 22.** Correlations between incoming (horizontal-axis) and outgoing (vertical-axis) translational velocity components in ( $\text{\AA}/\text{ps}$ ) and energy modes in (eV) of combined Fourier–Couette flow problem for  $\text{N}_2$ –Ni system at the bottom wall ( $S_w = 0.2$ ). The dashed horizontal and diagonal lines demonstrate fully diffusive and specular reflection, respectively. Solid red lines demonstrate the least-square linear fit of the kinetic data. In the last column, the corresponding probability density functions of the translational velocity components and energy modes for the reflecting particles are presented.

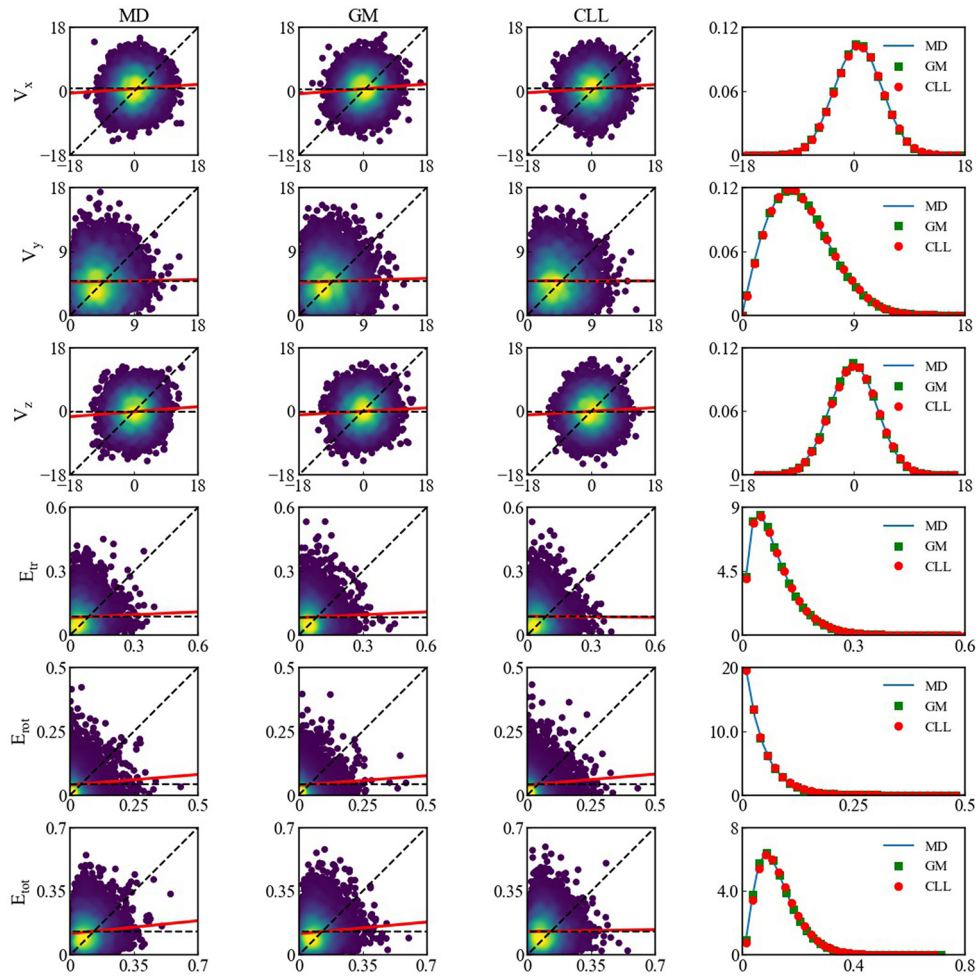


**FIG. 23.** Correlations between incoming (horizontal-axis) and outgoing (vertical-axis) translational velocity components in ( $\text{\AA}/\text{ps}$ ) and energy modes in (eV) of combined Fourier–Couette flow problem for  $N_2$ –Ni system at the top wall ( $S_v = 0.2$ ). The dashed horizontal and diagonal lines demonstrate fully diffusive and specular reflection, respectively. Solid red lines demonstrate the least-square linear fit of the kinetic data. In the last column, the corresponding probability density functions of the translational velocity components and energy modes for the reflecting particles are presented.

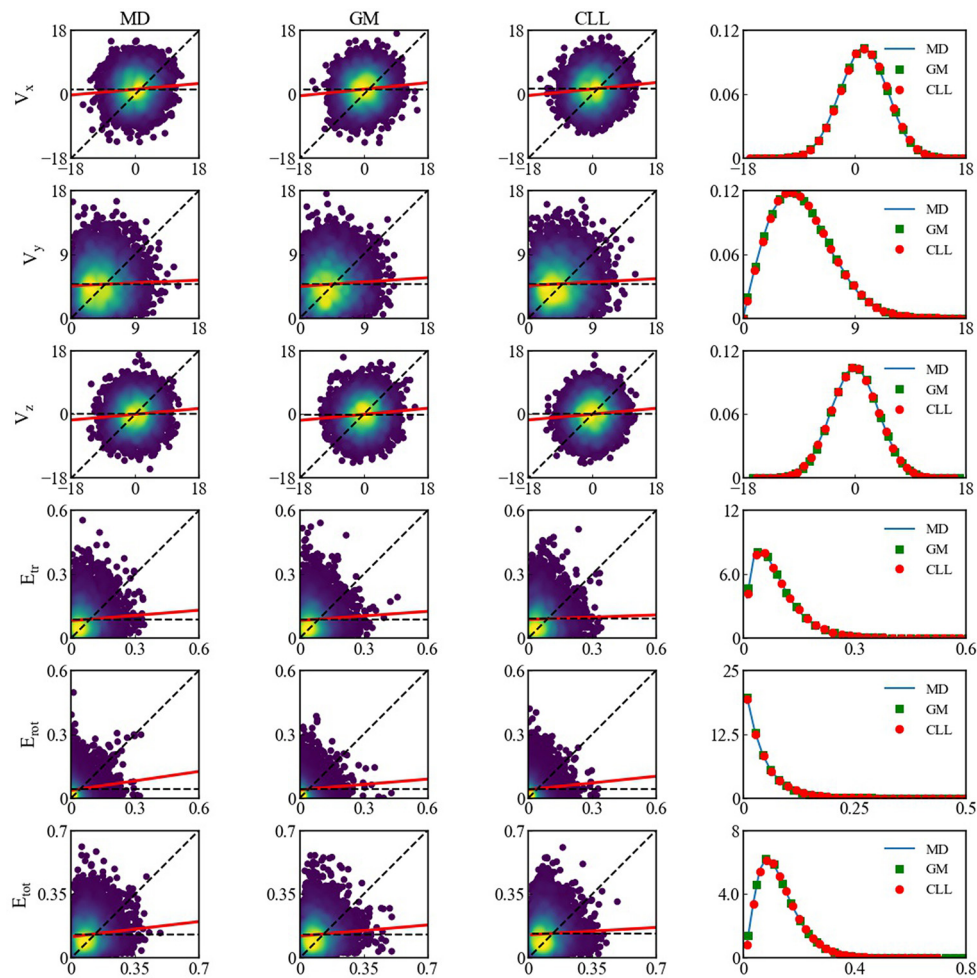


**FIG. 24.** Correlations between incoming (horizontal-axis) and outgoing (vertical-axis) translational velocity components in ( $\text{\AA}/\text{ps}$ ) and energy modes in (eV) of combined Fourier–Couette flow problem for  $\text{N}_2$ –Ni system at the top wall ( $S_v = 0.4$ ). The dashed horizontal and diagonal lines demonstrate fully diffusive and specular reflection, respectively. Solid red lines demonstrate the least-square linear fit of the kinetic data. In the last column, the corresponding probability density functions of the translational velocity components and energy modes for the reflecting particles are presented.

## REFERENCES

- <sup>1</sup>G. Karniadakis, A. Beskok, and N. Aluru, *Microflows and Nanoflows: Fundamentals and Simulation* (Springer Science and Business Media, 2006), Vol. 29.
- <sup>2</sup>C. Shen, *Rarefied Gas Dynamics: Fundamentals, Simulations and Micro Flows* (Springer Science and Business Media, 2006).
- <sup>3</sup>W.-M. Zhang, G. Meng, and X. Wei, “A review on slip models for gas microflows,” *Microfluid. Nanofluid.* **13**, 845–882 (2012).
- <sup>4</sup>X.-J. Gu and D. R. Emerson, “A high-order moment approach for capturing non-equilibrium phenomena in the transition regime,” *J. Fluid Mech.* **636**, 177–216 (2009).
- <sup>5</sup>G. A. Bird and J. Brady, *Molecular Gas Dynamics and the Direct Simulation of Gas Flows* (Clarendon Press Oxford, 1994), Vol. 5.
- <sup>6</sup>S. Chen and G. D. Doolen, “Lattice Boltzmann method for fluid flows,” *Annu. Rev. Fluid Mech.* **30**, 329–364 (1998).
- <sup>7</sup>J. C. Maxwell, “On stresses in rarefied gases arising from inequalities of temperature,” *Proc. R. Soc. London* **170**, 231–256 (1879).
- <sup>8</sup>M. Epstein, “A model of the wall boundary condition in kinetic theory,” *AIAA J.* **5**, 1797–1800 (1967).
- <sup>9</sup>C. Cercignani and M. Lampis, “Kinetic models for gas–surface interactions,” *Transp. Theory Stat. Phys.* **1**, 101–114 (1971).
- <sup>10</sup>R. Lord, “Application of the Cercignani–Lampis scattering kernel to direct simulation Monte Carlo calculations,” in *17th International Symposium on Rarefied Gas Dynamics, Aachen, Germany 1990*, edited by A. E. Beylich (VCH, Weinheim, Germany, 1990), pp. 1427–1433.
- <sup>11</sup>R. Lord, “Some extensions to the Cercignani–Lampis gas–surface scattering kernel,” *Phys. Fluids A* **3**, 706–710 (1991).
- <sup>12</sup>N. Yamanishi, Y. Matsumoto, and K. Shobatake, “Multistage gas–surface interaction model for the direct simulation monte carlo method,” *Phys. Fluids* **11**, 3540–3552 (1999).
- <sup>13</sup>K. Yamamoto, H. Takeuchi, and T. Hyakutake, “Characteristics of reflected gas molecules at a solid surface,” *Phys. Fluids* **18**, 046103 (2006).
- <sup>14</sup>A. Yakunchikov, V. Kovalev, and S. Utyuzhnikov, “Analysis of gas–surface scattering models based on computational molecular dynamics,” *Chem. Phys. Lett.* **554**, 225–230 (2012).
- <sup>15</sup>M. Hossein Gorji and P. Jenny, “A gas–surface interaction kernel for diatomic rarefied gas flows based on the Cercignani–Lampis–Lord model,” *Phys. Fluids* **26**, 122004 (2014).

- <sup>16</sup>A. Frezzotti and L. Gibelli, "A kinetic model for fluid-wall interaction," *Proc. Inst. Mech. Eng., Part C* **222**, 787–795 (2008).
- <sup>17</sup>P. Spijker, A. J. Markvoort, S. V. Nedea, and P. A. Hilbers, "Computation of accommodation coefficients and the use of velocity correlation profiles in molecular dynamics simulations," *Phys. Rev. E* **81**, 011203 (2010).
- <sup>18</sup>M. Barisik and A. Beskok, "Molecular dynamics simulations of shear-driven gas flows in nano-channels," *Microfluid. Nanofluid.* **11**, 611–622 (2011).
- <sup>19</sup>J. Sun and Z.-X. Li, "Three-dimensional molecular dynamic study on accommodation coefficients in rough nanochannels," *Heat Transfer Eng.* **32**, 658–666 (2011).
- <sup>20</sup>S. Mohammad Nejad, S. Nedea, A. Frijns, and D. Smeulders, "The influence of gas-wall and gas-gas interactions on the accommodation coefficients for rarefied gases: A molecular dynamics study," *Micromachines* **11**, 319 (2020).
- <sup>21</sup>D. Bruno, M. Cacciatore, S. Longo, and M. Rutigliano, "Gas-surface scattering models for particle fluid dynamics: A comparison between analytical approximate models and molecular dynamics calculations," *Chem. Phys. Lett.* **320**, 245–254 (2000).
- <sup>22</sup>Z. Liang and P. Kebllinski, "Parametric studies of the thermal and momentum accommodation of monoatomic and diatomic gases on solid surfaces," *Int. J. Heat Mass Transfer* **78**, 161–169 (2014).
- <sup>23</sup>B.-Y. Cao, J. Sun, M. Chen, and Z.-Y. Guo, "Molecular momentum transport at fluid-solid interfaces in MEMS/NEMS: A review," *Int. J. Mol. Sci.* **10**, 4638–4706 (2009).
- <sup>24</sup>S. C. Saxena and R. K. Joshi, *Thermal Accommodation and Adsorption Coefficients of Gases* (McGraw-Hill, New York, NY, 1981).
- <sup>25</sup>M. Liao, Q.-D. To, C. Léonard, and V. Monchiet, "Non-parametric wall model and methods of identifying boundary conditions for moments in gas flow equations," *Phys. Fluids* **30**, 032008 (2018).
- <sup>26</sup>N. Andric, D. W. Meyer, and P. Jenny, "Data-based modeling of gas-surface interaction in rarefied gas flow simulations," *Phys. Fluids* **31**, 067109 (2019).
- <sup>27</sup>W. Liu, J. Zhang, Y. Jiang, L. Chen, and C.-H. Lee, "DSMC study of hypersonic rarefied flow using the Cercignani-Lampis-Lord model and a molecular-dynamics-based scattering database," *Phys. Fluids* **33**, 072003 (2021).
- <sup>28</sup>M. Liao, Q.-D. To, C. Léonard, and W. Yang, "Prediction of thermal conductance and friction coefficients at a solid-gas interface from statistical learning of collisions," *Phys. Rev. E* **98**, 042104 (2018).
- <sup>29</sup>S. M. Nejad, E. Iype, S. Nedea, A. Frijns, and D. Smeulders, "Modeling rarefied gas-solid surface interactions for Couette flow with different wall temperatures using an unsupervised machine learning technique," *Phys. Rev. E* **104**, 015309 (2021).
- <sup>30</sup>H. Wu, W. Chen, and Z. Jiang, "Gaussian mixture models for diatomic gas-surface interactions under thermal non-equilibrium conditions," *Phys. Fluids* **34**, 082007 (2022).
- <sup>31</sup>P. Atkins and J. D. Paula, *Physical Chemistry for the Life Sciences* (Oxford University Press, 2011).
- <sup>32</sup>S. Foiles, M. Baskes, and M. S. Daw, "Embedded-atom-method functions for the FCC metals Cu, Ag, Au, Ni, Pd, Pt, and their alloys," *Phys. Rev. B* **33**, 7983 (1986).
- <sup>33</sup>H. Sun, "Compass: An *ab initio* force-field optimized for condensed-phase applications overview with details on alkane and benzene compounds," *J. Phys. Chem. B* **102**, 7338–7364 (1998).
- <sup>34</sup>J. Yang, Y. Ren, A. m Tian, and H. Sun, "Compass force field for 14 inorganic molecules, He, Ne, Ar, Kr, Xe, H<sub>2</sub>, O<sub>2</sub>, N<sub>2</sub>, NO, CO, CO<sub>2</sub>, NO<sub>2</sub>, CS<sub>2</sub>, and SO<sub>2</sub>, in liquid phases," *J. Phys. Chem. B* **104**, 4951–4957 (2000).
- <sup>35</sup>M. Waldman and A. T. Hagler, "New combining rules for rare gas van der Waals parameters," *J. Comput. Chem.* **14**, 1077–1084 (1993).
- <sup>36</sup>W. G. Hoover, "Canonical dynamics: Equilibrium phase-space distributions," *Phys. Rev. A* **31**, 1695 (1985).
- <sup>37</sup>S. Plimpton, "Fast parallel algorithms for short-range molecular dynamics," *J. Comput. Phys.* **117**, 1–19 (1995).
- <sup>38</sup>V. Chirita, B. Pailthorpe, and R. Collins, "Molecular dynamics study of low-energy Ar scattering by the Ni (001) surface," *J. Phys. D: Appl. Phys.* **26**, 133 (1993).
- <sup>39</sup>G. J. McLachlan and K. E. Basford, *Mixture Models: Inference and Applications to Clustering* (M. Dekker, New York, 1988), Vol. 38.
- <sup>40</sup>D. A. Reynolds and R. C. Rose, "Robust text-independent speaker identification using Gaussian mixture speaker models," *IEEE Trans. Speech Audio Process.* **3**, 72–83 (1995).
- <sup>41</sup>M. Raitoharju, Á. F. García-Fernández, R. Hostettler, R. Piché, and S. Särkkä, "Gaussian mixture models for signal mapping and positioning," *Signal Process.* **168**, 107330 (2020).
- <sup>42</sup>L. Li, R. J. Hansman, R. Palacios, and R. Welsch, "Anomaly detection via a Gaussian mixture model for flight operation and safety monitoring," *Transp. Res. Part C: Emerging Technol.* **64**, 45–57 (2016).
- <sup>43</sup>A. P. Dempster, N. M. Laird, and D. B. Rubin, "Maximum likelihood from incomplete data via the EM algorithm," *J. R. Stat. Soc.: Ser. B* **39**, 1–22 (1977).
- <sup>44</sup>F. Pedregosa, G. Varoquaux, A. Gramfort, V. Michel, B. Thirion, O. Grisel, M. Blondel, P. Prettenhofer, R. Weiss, V. Dubourg *et al.*, "Scikit-learn: Machine learning in python," *J. Mach. Learn. Res.* **12**, 2825–2830 (2011).
- <sup>45</sup>W. Trott, D. Rader, J. Castaneda, J. Torczynski, and M. Gallis, "Experimental measurements of thermal accommodation coefficients for microscale gas-phase heat transfer," AIAA Paper No. 2007-4039, 2007.
- <sup>46</sup>A. Agrawal and S. Prabhu, "Survey on measurement of tangential momentum accommodation coefficient," *J. Vac. Sci. Technol., A* **26**, 634–645 (2008).
- <sup>47</sup>I. Amdur and L. Guildner, "Thermal accommodation coefficients on gas-covered tungsten, nickel and platinum," *J. Am. Chem. Soc.* **79**, 311–315 (1957).
- <sup>48</sup>Q. Wang, S. R. Kulkarni, and S. Verdú, "Divergence estimation of continuous distributions based on data-dependent partitions," *IEEE Trans. Inf. Theory* **51**, 3064–3074 (2005).
- <sup>49</sup>V. Chirita, B. Pailthorpe, and R. Collins, "Non-equilibrium energy and momentum accommodation coefficients of Ar atoms scattered from Ni (001) in the thermal regime: A molecular dynamics study," *Nucl. Instrum. Methods Phys. Res., Sect. B* **129**, 465–473 (1997).
- <sup>50</sup>T. Liang, Q. Li, and W. Ye, "Performance evaluation of Maxwell and Cercignani-Lampis gas-wall interaction models in the modeling of thermally driven rarefied gas transport," *Phys. Rev. E* **88**, 013009 (2013).
- <sup>51</sup>N. Uene, H. Takeuchi, Y. Hayamizu, and T. Tokumasu, "Study of reflection models of gas molecules on water adsorbed surfaces in high-speed flows," *J. Fluid Sci. Technol.* **15**, JFST0005 (2020).
- <sup>52</sup>A. J. Markvoort, P. Hilbers, and S. Nedea, "Molecular dynamics study of the influence of wall-gas interactions on heat flow in nanochannels," *Phys. Rev. E* **71**, 066702 (2005).
- <sup>53</sup>J. Sun and Z.-X. Li, "Effect of gas adsorption on momentum accommodation coefficients in microgas flows using molecular dynamic simulations," *Mol. Phys.* **106**, 2325–2332 (2008).